# ENGINEERING OF DIAMOND BASED SENSOR FOR NANO-SCALE MAGNETIC FIELD SOURCES

A Dissertation

by

FAHAD SULAYMAN M. ALGHANNAM

Submitted to the Office of Graduate and Professional Studies of
Texas A&M University
in partial fulfillment of the requirements for the degree of

DOCTOR OF PHILOSOPHY

| | |
|---|---|
| Chair of Committee, | M. Suhail Zubairy |
| Co-Chair of Committee, | Philip Hemmer |
| Committee Members, | Aleksei M Zheltikov |
| | Alexei Sokolov |
| Head of Department, | Peter McIntyre |

May 2018

Major Subject: Physics

## ABSTRACT

Diamond-based magnetometry utilizes the negatively charged nitrogen-vacancy color center NV. For sensing nano-scale magnetic field sources, the small size of the NV is a great advantage over other magnetometers. However, conventional implantation and growth techniques fail to produce very shallow NVs which can be brought to close proximity of small magnetic field sources. Here, we investigate innovative implantation and growth techniques to address this problem.

For bulk diamond, we were able to create a concentrated layer of NVs approximately 2nm for the diamond surface. Direct measurement of magnetic sensitivity for this layer yields a sensitivity of $125nT\mu m^{3/2}/\sqrt{Hz}$. For currents running in nano-scale wires on the diamond surface this translates to sensitivities below $fA/\sqrt{Hz}$ .

To produce superior nanodiamond magnetic sensor, we attempt growth of fluorescent nanodiamonds using two methods, High-Pressure-High-Temperature (HPHT), and plasma enhanced chemical vapor deposition CVD. We show results for fluorescent nanodiamond grown around 1-adamantylamine seed molecule. We show that the nitrogen in the seed molecule was successfully transformed to NV through electron irradiation at high temperature. Also, we show results of fluorescent nanodiamonds grown using a home built plasma CVD system. Nitrogen was introduced to the diamond by adding trimethylamine to the reactor chamber. Once again, the diamond was not fluorescent until after electron irradiation at high temperature.

CONTRIBUTORS AND FUNDING SOURCES

## Contributors

This work was supported by a dissertation committee consisting of Professor M. Suhail Zubairy [advisor] and Professors Aleksei M Zheltikov and Alexei Sokolov of the Department of Physics and Professor Philip Hemmer [co-advisor] of the Department of Electrical and Computer Engineering.

The HPHT growth was preformed in Carnegie institution for Science by Todd Zapata. The palsma CVD growth was preformed in our lab by Abdurrahman Almethen.

All other work conducted for the dissertation was completed by the student independently.

## Funding Sources

Graduate study was supported by a scholarship from King Abdulaziz City for Science and Technology (KACST).

TABLE OF CONTENTS

Page

LIST OF FIGURES

FIGURE Page

# 1. INTRODUCTION

## 1.1 Motivation and Applications

Despite the major progress in magnetometry in the last few decades, currently available magnetometers do not meet the minimum requirements for many applications in science and technology. Even though magnetic sensors with sensitivities of the order of $aT/\sqrt{Hz}$ has been reported, none of them can be brought to the proximity of a nano-scale magnetic field source (i.e., electrical current or a magnetic dipole) while maintaining the high sensitivity performance. Figure(1.1) shows a some of the available magnetic sensors distributed according to their sensitivity and size.

Diamond-based magnetic sensors utilize optically active color centers in the diamond lattice for sensing purposes. The diamond lattice has an indirect energy gap of 5.5eV. Such a large energy gap leads to the existence of countless optically active deep defects in diamond. Among these defects, the most famous one, especially for sensing applications, is the nitrogen-vacancy center.

## 1.2 The Nitrogen-Vacancy in Diamond

The NV center in diamond is a complex defect consisting of a substitutional nitrogen next to a vacancy in the diamond lattice. The NV has two stable charge states neutral $NV^0$ and negatively charged $NV^-$. Throughout this document, NV will stand for the negatively charged NV.

Figure (1.2a) shows the energy level diagram for the NV. The ground state is a spin triplet with zero field splitting (ZFS) D = 2.87GHz. The excited state is a spin triplet as well with ZFS D=1.4GHz. Typically, NVs are excited with green laser and has a red emission with a zero phonon line at 638nm and a wide phonon side band, figure(1.2b).

One of the most attractive attributes of the NV is that it is possible to read out the spin

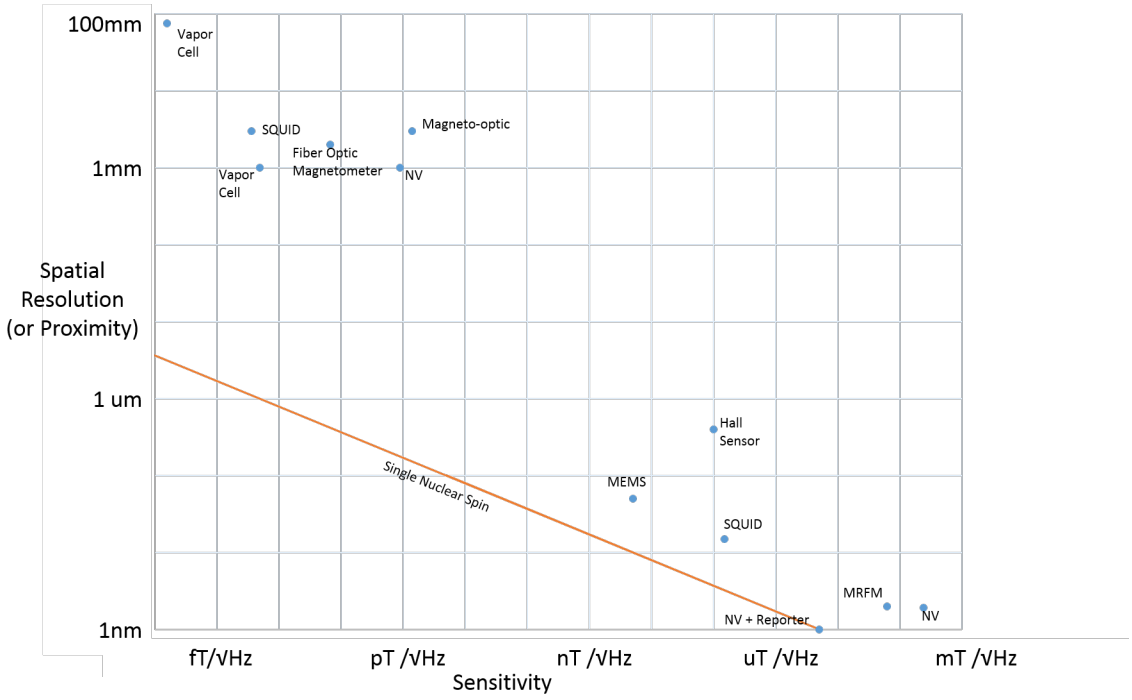


Figure 1.1: Some of the currently available magnetometers displayed in terms of magnetic sensitivity and spatial resolution (or size): Vapor Cell [1][2], SQUID [3][4], Fiber Optic Magnetometer[5], Magneto-optic[6], NV diamond [7][8], MEMS, MRFM[9], NV with Quantum Reporter [10].

state optically. This phenomenon is often called Optically Detected Magnetic Resonance ODMR. When an NV in state $m_s = 0$ is optically excited, it relaxes to the ground state by emitting a red photon. In contrast, when an NV in states $m_s = +1$ or $m_s = -1$ is optically excited, there is a $30\%$ probability that the NV will relax through a non-radiative path. This non-radiative decay process ultimately leads to a dip in NV fluorescence Figure(1.2c).

Single NVs, as well as NV ensembles, were used to measure magnetic field sources. For example, a thick layer of NVs was used to measure the magnetic field of a single neuron action potential of an earthworm[11]. Also, single NVs and a thin layer of NVs were used to demonstrate NMR spectroscopy[12]. Furthermore, by coupling a relatively shallow single NV to dark spins on the surface of the diamond, sensing, and localization

of a single nuclear spin was demonstrated[10].

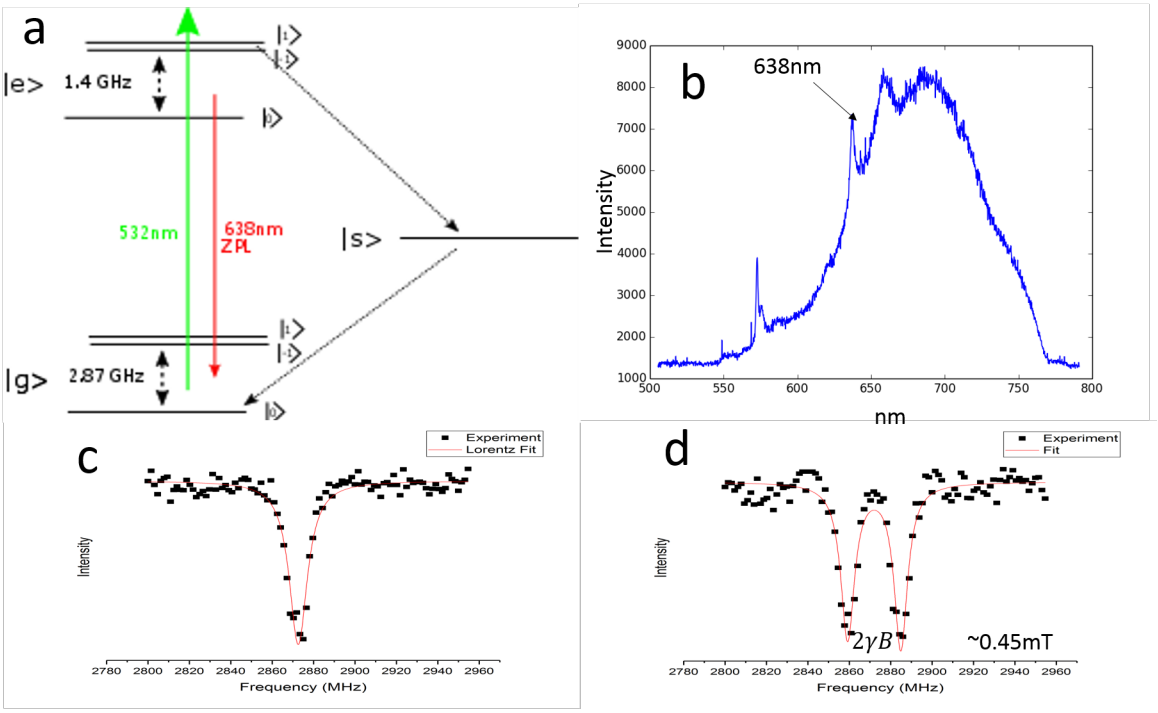


Figure 1.2: a) Energy diagram of the NV showing the zero field splitting of the ground and the excited states. b) An optical spectrum of the NV showing the ZPL at 638nm. c) An ODMR spectrum of the NV's ground state. d) An ODMR spectrum of the NV's ground state with a magnetic field of 0.45mT.

## 1.3 NV's Sensing Protocols

### 1.3.1 Continuous Wave Experiments

The spin Hamiltonian of the NV's ground state is given by equation (1.1). When the NV is placed in an axial magnetic field, the Zeeman term in the Hamiltonian splits the states $m_s = +1$ and $m_s = -1$ . This splitting equals $2\gamma B$ and is optically detectable through the ODMR phenomenon, Figure (1.2d). By fitting the ODMR spectrum of the

NV, the magnetic field is measured. Here the sensitivity of the measurement is limited by the peak width which is determined by the NV's dephasing time $T_2^*$.

$$H = \underbrace{\hbar D(S_z^2 - \frac{2}{3})}_{\text{ZFS}} + \underbrace{\gamma B \cdot S}_{\text{Zeeman term}} \tag{1.1}$$

### 1.3.2 Pulsed Experiments

Pulsed experiments are technically more challenging than CW but they have a few advantages. For DC field sensing the Ramsey pulse sequence is usually implemented. In Ramsey experiments, the NV is prepared in $m_s = 0$ state using an initialization laser pulse. Then a $\pi/2$ MW pulse is applied to send the NV to a superposition state. At this stage the NV is dephasing and the accumulated phase depends on the magnetic field. After time $\tau$, another $\pi/2$ pulse is applied to map the phase into $m_s = 0$ population and an optical read out pulse is used to measure the accumulated phase. By scanning the dephasing time $\tau$, an optical Ramsey spectrum is generated and fitting the spectrum yields the value of the magnetic field. Like CW experiments the Ramsey experiment is also limited by $T_2^*$. However, it has an advantage over CW experiments in that it overcomes power broadening issues.

True benefit of pulse experiments is for AC magnetic field sensing. In such experiments, the Hahn-echo pulse sequence is usually implemented. This pulse sequence is the same as Ramsey's pulse sequence but with an additional $\pi$ pulse between the two $\pi/2$ pulses. In this case, if the period of the AC magnetic field is equal to the dephasing time $\tau$, then the accumulated phase directly depends on the amplitude of the AC field. This echo experiment has the great advantage that it is not limited by the dephasing time $T_2^*$ but by the spin-spin relaxation time $T_2$, which can be orders of magnitude higher than $T_2^*$.

### 1.3.3 Relaxometry

Relaxometry is a sensing technique where the relaxation time $T_1$ of the NV is monitored to measure the magnetic field signal at the spin transition frequency. This protocol is usually reserved for high-frequency applications like sensing electronic spin magnetic resonance. It also has the advantage of not requiring microwaves which may be vital for some applications where a microwave field might destroy the sample.

## 1.4 Dissertation Outline

In chapter 2 we discuss the magnetic sensitivity of an NV ensemble. We also show the difference between magnetic field sensitivity and sensitivity to a magnetic field source. We discuss two examples in details showing the relation of sensitivity to proximity and spatial resolution.

In chapters 3 and 4, the experimental setups used in this research is explained. In chapter 3, we talk specifically about sensor's manufacturing setups. We discuss in details our home built implantation system and MW plasma nanodiamond growth system. In chapter 4, we give details about our home built confocal microscope and about the use of electron microscopy for imaging and irradiation.

In chapters 5 and 6, the results of this work are presented. In chapter 5 we show results for shallow layers of NVs in bulk diamond. In chapter 6, results for nanodiamond growth using HPHT and MW plasma are presented. Finally, in chapter 7 we give a short summary and discuss further studies on this topic.

# 2. NV SENSITIVITY

## 2.1 Magnetic Sensitivity

Magnetic sensitivity of an ensemble of NVs is directly related to how well the center of the ODMR peaks can be located. This depends on the peak's contrast $\eta$ and its half width at half maximum $a$. It also depends on the measurement's signal to noise ratio SNR. At the shot noise limit, SNR depends on the photon count rate and the integration time. We can calculate the magnetic sensitivity of an ensemble of NVs by analyzing the change in fluorescence intensity due to the magnetic field. The fluorescence intensity $I$ is given by:

$$I = I_{NV} t \rho_{NV} \int (1 - \frac{\eta}{1 + (\frac{\omega - D - \gamma B_z}{a})^2}) dV \tag{2.1}$$

Where:

$\mathrm{I}_{NV}$ = Intensity of a single NV per unit time

$\rho_{NV}$ = Density of NVs per unit volume

$\eta$ = ODMR peak Contrast

$t$ = integration time

$a$ = Half Width at Half Maximum

$\gamma$ = $28GHz/T$ is the magnetic field couping coefficient of the NV

$\mathrm{B}_z$ = The magnetic field parallel to the NV axis

D = $2.87GHz$ is the zero field splitting of the NV's ground state

For $B_z << \frac{a}{\gamma}$

$$\Delta I = I - I(B_z = 0) = -I_{NV} t \rho_{NV} \int \frac{2\gamma\eta(\omega - D)/a}{a(1 + (\frac{\omega - D}{a})^2)} B_z dV \tag{2.2}$$

Maximum sensitivity is achieved by tuning the microwave excitation to the steepest slope of the fluorescence intensity ($\omega = D \pm \frac{a}{\sqrt{3}}$). Here the change in fluorescence intensity is:

$$\Delta I = \mp \frac{9\gamma\eta}{8\sqrt{3}a} I_{NV} t \rho_{NV} \int B_z dV \tag{2.3}$$

Assuming the measurement is only limited by shot noise = $\sqrt{I_{NV}\rho_{NV}V}$ The signal to noise ratio is given by:

$$SNR = \frac{9\gamma\eta}{8\sqrt{3}a} \sqrt{\frac{I_{NV} t \rho_{NV}}{V}} \int B_z dV \tag{2.4}$$

If we assume a uniform magnetic field, the sensitivity is:

$$\Delta B = \frac{8\sqrt{3}a}{9\gamma\eta} \frac{1}{\sqrt{I_{NV} t \rho_{NV} V}} \tag{2.5}$$

We can define the sensitivity in a unit volume and unit time to be:

$$\delta B = \frac{8\sqrt{3}a}{9\gamma\eta} \frac{1}{\sqrt{I_{NV}\rho_{NV}}} \tag{2.6}$$

From equation(2.6), sharper ODMR peaks are desired to increase magnetic sensitivity. Ignoring avoidable effects, like power broadening, the ODMR peak width is inversely related to the relaxation time $T_2$ of the NV or $T_2^*$ in CW experiments. The value of $T_2$ depends on the quality of the diamond lattice in the vicinity on the NV. Sources of magnetic noise, like substitutional nitrogen atoms, carbon 13 nuclear spin, or even other NVs,

will inevitably reduce $T_2$. Therefore, highest $T_2$ values are found in single NVs in carbon 12 enriched ultra-pure diamond substrates[13]. However, this does not translate to highest magnetic sensitivity, since using a single NV means a low photon count rate when compared to NV ensembles.

To increase the magnetic sensitivity, brightness is increased by incorporating more NVs in the region of interest. To keep the ODMR sharp, thick layers of relatively low concentrations of NVs are generally used. Even though such layers give superior sensitivity, they suffer from low spatial resolution , so they cannot be used for sensing nano-scale magnetic field sources.

## 2.2 Sensitivity, Spatial Resolution, and Proximity

Sensitivity to magnetic fields is not equivalent to sensitivity to magnetic field sources. Since a magnetic field of an electrical current drops as $1/r$ and that of a magnetic dipole drops as $1/r^3$, it is imperative to get the sensor as close as possible to the source even at the expense of sensitivity. Furthermore, for most sensing applications, a spatial map (image) of the field sources is desirable. The spatial resolution of such images is ultimately limited by the sensor's size and proximity. To illustrate the effect of geometrical parameters of the NVs layer on sensitivity for different sources we calculate the sensitivity to a current in a long wire and to a magnetic dipole.

### 2.2.1 Example 1: Magnetic Field Due to an Electrical Current in a Long Wire

In this example, we want to calculate the sensitivity of a layer of NVs to a magnetic field generate by a current $I$ running through a wire with radius $R$ that is much longer than the region of interest. The geometry of this problem is illustrated in figure(2.1). The magnetic field outside the wire is

$$B = \frac{\mu_0 I}{2\pi\sqrt{x^2 + z^2}} \tag{2.7}$$

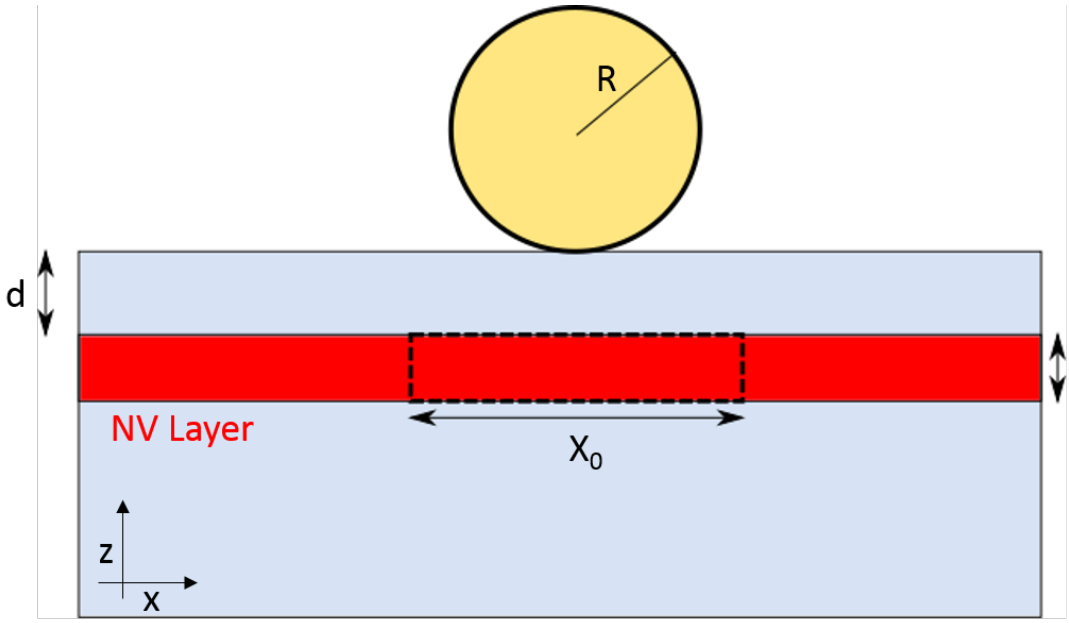


Figure 2.1: A diagram showing the geometry of the long wire example

Since NVs are sensitive to magnetic fields along the NV axis, we calculate the field's projection along the axis of one of the NV sub ensembles to be:

$$B = \frac{\mu_0 I}{2\pi} \frac{zsin\alpha + xcos\alpha}{x^2 + z^2} cos\beta \tag{2.8}$$

Where

$\alpha =$ is the angle of the NV axis with the z axis

$\beta =$ is the angle of the projection of the NV axis on the xy plan with the x axis

The limiting dimension of this problem is the wire radius $R$, therefore it is useful to use distances in units of $R$, and so the field becomes:

$$B = \frac{\mu_0 I}{2\pi R} \frac{zsin\alpha + xcos\alpha}{x^2 + z^2} cos\beta \tag{2.9}$$

The current sensitivity $\delta I$ will be:

$$\delta I = \delta B \frac{2\pi R}{\mu_0} \sqrt{\frac{1}{t y_0}} G_I(d, x_0, T) \tag{2.10}$$

Equation (2.10) gives the current sensitivity in terms of the magnetic sensitivity modified by a geometrical factor $G_I$ which is a function of the depth $d$, the thickness $T$, and the dimension of the integration volume $x_0$ which also represents the spatial resolution of this problem. To illustrate this problem further we choose the case $\alpha = \pi/2$ and $\beta = 0$ and we assume a rectangular region of interest, then the function $G_I$ is:

$$G_I(d, x_0, T) = \frac{\sqrt{x_0 T}}{\int_{-x_0/2}^{x_0/2} \int_{d+1}^{T+d+1} \frac{z}{x^2 + z^2} dz dx} \tag{2.11}$$

We substitute for $G_I$ in equation(2.10) and we get:

$$\frac{\delta I}{R} = \delta B \frac{2\pi}{\mu_0} \sqrt{\frac{x_0 T}{t y_0}} \frac{1}{\int_{-x_0/2}^{x_0/2} \int_{d+1}^{T+d+1} \frac{z}{x^2 + z^2} dz dx} \tag{2.12}$$

In figure (2.2) we depict equation (2.12) for $d = 0$, $d = R$, and $d = 10R$ and the X and Y axes are in units of the radius $R$. From these plots we notice three important conclusions. First, as expected, increasing the depth $d$ degrades sensitivity and spatial resolution significantly. Second, sensitivity is always highest near the line $x_0 = T$. Third, Increasing the integration area $x_0 \times T$ increases the sensitivity until it reaches a saturation value, after which, further increase in the integration area degrades spatial resolution without any gain in sensitivity.

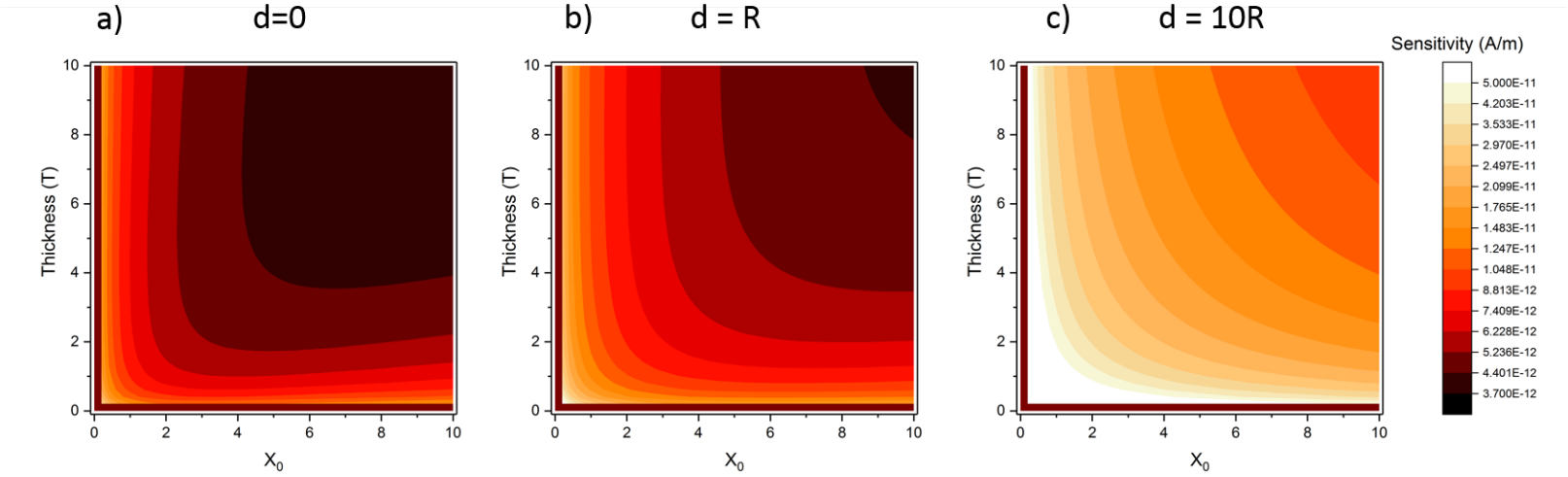


Figure 2.2: The sensitivity to a magnetic field generated by current in a long wire normalized by the wire radius for an NV layer with depth a) $d = 0$, b) $d = R$, and c) $d = 10R$. The Y axis is the layer's thickness and the X axis is the resolution as illustrated in figure(2.1). We assume the magnetic sensitivity of the NV layer $\delta B = 2.3nT\mu m^{3/2}/\sqrt{Hz}$ and an integration time of 1 second.

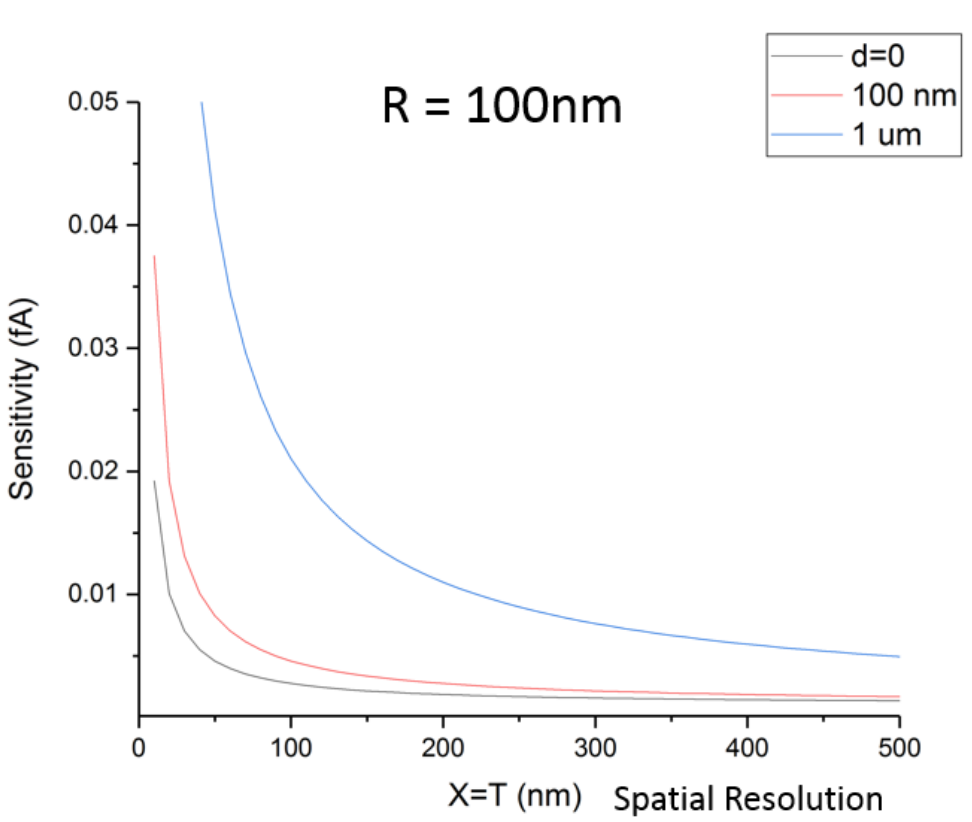


Figure 2.3: Sensitivity of an NV layer to a current running in a wire with a $100nm$ radius on the diamond's surface for different depths $d = 0$, $d = 100nm$, and $d = 1\mu m$. We assume the magnetic sensitivity of the NV layer $\delta B = 2.3nT\mu m^{3/2}/\sqrt{Hz}$ and an integration time of 1 second.

### 2.2.2 Example 2: Magnetic Field of a Magnetic Dipole

In this example, we want to calculate the sensitivity of a layer of NVs to a magnetic field generated by a magnetic dipole moment. In this example the magnetic field rolls off as $1/r^3$ much faster than the first example. First, we assume the magnetic dipole has the same direction as the axes of the NV ensemble. This assumption is practical for cases like nuclear dipoles and atomic dipoles since the dipoles are usually aligned using an external field which is in the direction of the quantization axes of the NVs. The geometry of this

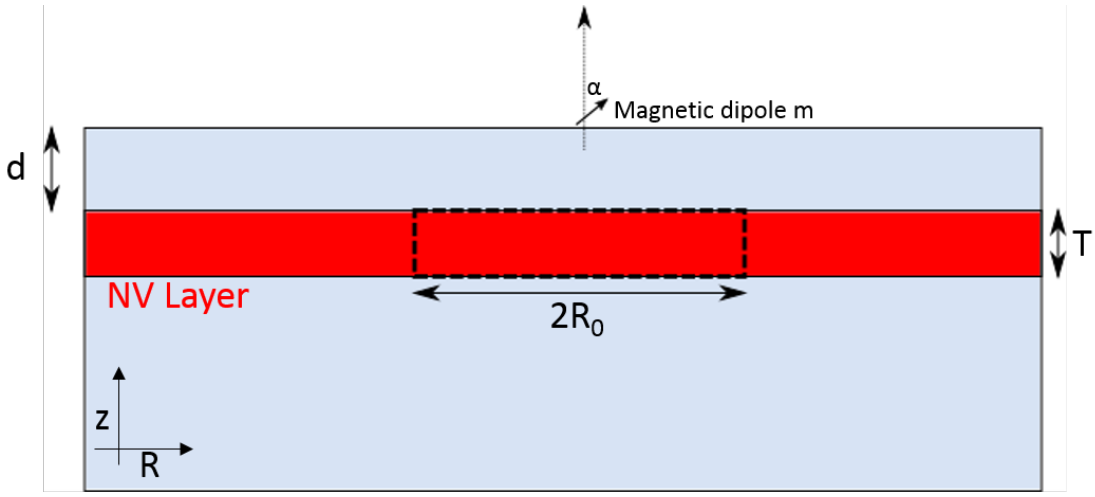


Figure 2.4: A diagram showing the geometry of magnetic dipole example

problem is illustrated in figure(2.4). The projection of the magnetic field of a dipole on the surface of the diamond on the NV axes is

$$B = \frac{\mu_0 m}{4\pi}[\frac{3(zcos\alpha + Rsin\alpha)^2}{(z^2+R^2)^{5/2}} - \frac{1}{(z^2+R^2)^{3/2}}] \tag{2.13}$$

Where

m = is the magnetic dipole moment

$\alpha$ = is the angle of the dipole m (and the NV axes) with z

$\mu_0$ = is the magnetic permeability

From this we can calculate the sensitivity to the magnetic dipole moment $\delta m$

$$\delta m = \delta B \frac{2}{\mu_0}\sqrt{\frac{1}{t}} G_m(d, R_0, T) \tag{2.14}$$

Similar to the case of the current sensitivity, equation (2.14) gives the sensitivity to the magnetic dipole moment in terms of the magnetic sensitivity modified by a geometrical factor $G_m$. $G_m$ is a function of the depth $d$, the thickness $T$, and the radius of the integra-

tion volume $R_0$, which represents the spatial resolution of this problem. To illustrate this problem further we choose the case $\alpha = 0$ and we assume a cylindrical region of interest, then the function $G_m$ becomes:

$$G_m(d, R_0, T) = \frac{\sqrt{\pi R_0^2 T}}{\int_d^{T+d} \int_0^{R_0} [\frac{3z^2 R}{(z^2+R^2)^{5/2}} - \frac{R}{(z^2+R^2)^{3/2}}] dR dz} \tag{2.15}$$

We substitute for $G_m$ in equation(2.14) and we get:

$$\delta m = \delta B \frac{2}{\mu_0} \sqrt{\frac{1}{t}} \frac{\sqrt{\pi R_0^2 T}}{\int_d^{T+d} \int_0^{R_0} [\frac{3z^2 R}{(z^2+R^2)^{5/2}} - \frac{R}{(z^2+R^2)^{3/2}}] dR dz} \tag{2.16}$$

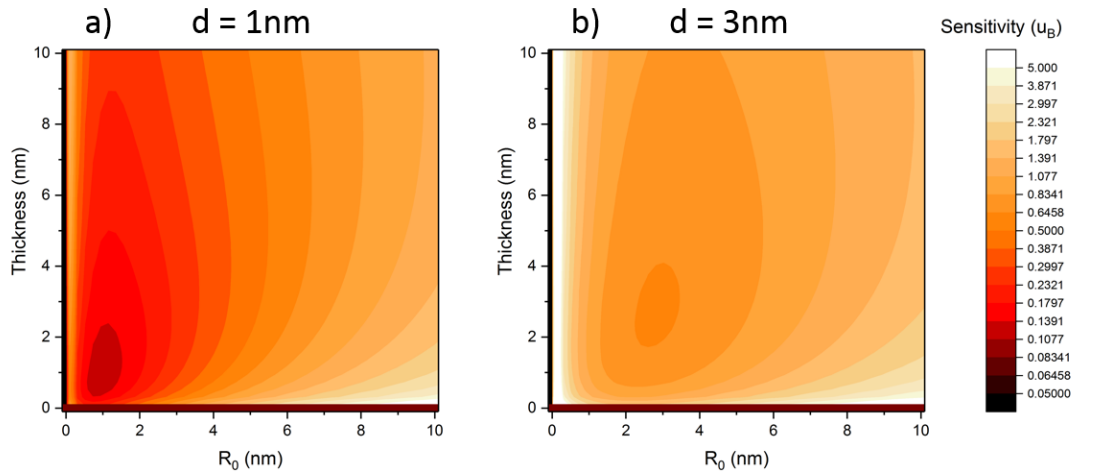


Figure 2.5: The sensitivity to a magnetic field generated by a magnetic dipole on the diamond's surface for an NV layer with depth a) $d = 1nm$, and b) $d = 3nm$. The Y axis is the layer's thickness and the X axis is the spatial resolution as illustrated in figure(2.4). We assume the magnetic sensitivity of the NV layer $\delta B = 2.3nT\mu m^{3/2}/\sqrt{Hz}$ and an integration time of 1 second.

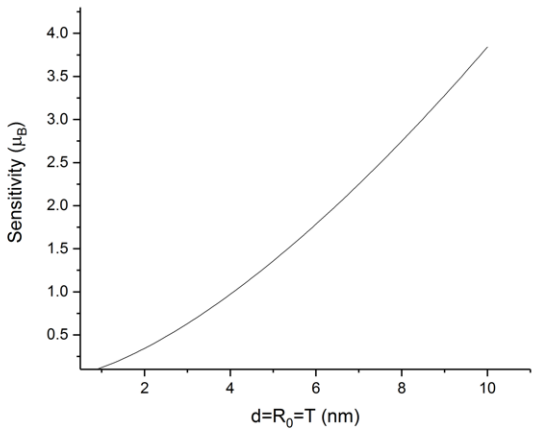


Figure 2.6: The maximum sensitivity of a layer of NVs to a magnetic dipole moment on the diamond's surface as a function of the layer's depth

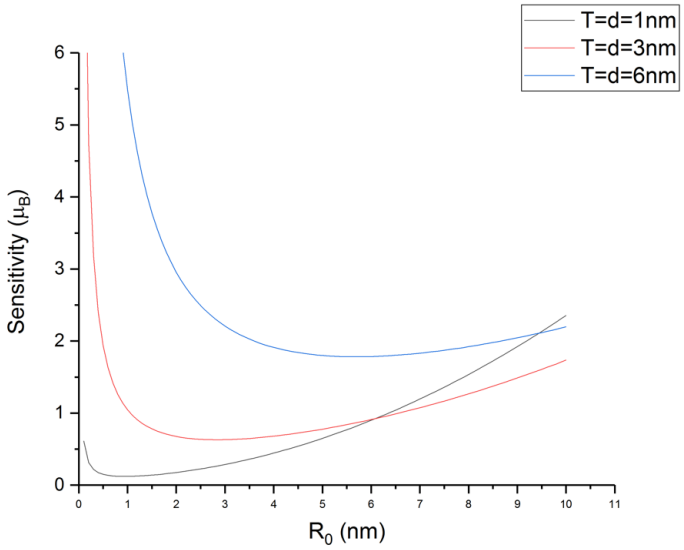


Figure 2.7: The sensitivity of a layer of NVs to a magnetic dipole moment on the diamond's surface as a function of the layer's spot radius $R_0$ for different layer depth d and thickness T.

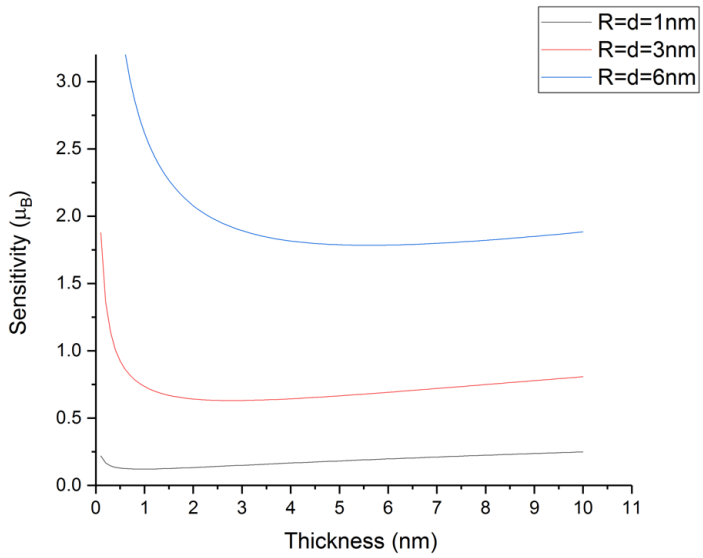


Figure 2.8: The sensitivity of a layer of NVs to a magnetic dipole moment on the diamond's surface as a function of the layer's Thickness $T$ for different layer depth d and spatial resolution $R_0$.

In figure (2.5) we depict equation (2.16) for depths $d = 1nm$ and $d = 3nm$. We can see that the maximum sensitivity in each case is when $d = T = R_0$. This prompts us to plot the maximum sensitivity as a function of depth, namely at the point $d = T = R_0$, figure(2.6). As expected, the maximum sensitivity to a magnetic dipole degrades rapidly as the depth increases. We also notice that super-resolution microscopy might be essential for some applications not only for high spatial resolution but also for high SNR.

## 2.3 Conclusion

### 2.3.1 Layer Thickness and Integration Volume

From the two examples discussed earlier, best choice of thickness and integration volume depends on the targeted application. In general, creating NV layers with thicknesses up to a few hundred nanometers is not a problem. As for integration volume, laser spot sizes less than the diffraction limit ($\sim 250nm$) is possible through super-resolution mi-

croscopy techniques. For example, the spatial resolution of around 10nm was demonstrated on NVs using stimulated emission depletion STED microscopy [14]. Other techniques like tip enhancement and structured illumination could be utilized as well.

### 2.3.2 NV's Optimum Depth and Limitations

From the previous discussion, very shallow NV layers are most sensitive to nanoscale sources. However, commonly used implantation and growth techniques fail to create good quality layers near the diamond's surface due to surface termination problems and subsurface damage. Near the surface, negatively charged NVs are unstable since they lose an electron to nearby electron traps and neutrally charged NVs is the most stable charge state. Even in cases where some negatively charged NVs survive, their sensitivity suffers greatly due to unpaired electron spins on the diamond's surface or in the subsurface damage. We propose an innovative implantation technique to create high-quality shallow layers of NVs that surpass the performance of currently available NV layers.

Also, we can consider NVs in very small nanodiamonds to have a depth less than the nanoparticle's radius. However, the smallest nanodiamond with $NV^-$ is 10nm in diameter and suffers from low sensitivity due to the low quality of the crystal. For this, we are developing a seeded growth technique which should lead to smaller nanodiamonds with NVs with higher magnetic sensitivity.

# 3. APPROACH AND EXPERIMENTAL METHODS

## 3.1 Implantation

In physics and material science, implantation is the process of introducing a foreign element into a crystalline substrate by accelerating ions of that element and colliding it with the substrate. Typically, a gas of the desired element is ionized in a separate chamber; then the ions are extracted and accelerated toward the substrate in the implantation chamber. Implanting nitrogen in a diamond substrate was one of the first methods used to create NVs. Usually, a nitrogen implantation step is used to create both nitrogen defects and vacancies in the diamond lattice. Then, post-implantation annealing diffuses the vacancies until they trapped by substitutional nitrogen defects thus forming NVs.

A disadvantage of implantation is that every implanted atom leaves a trail of damage in the lattice. Although annealing may cure some of the damage, long chain of vacancies, most likely near the surface, are almost impossible to cure. Therefore, creating shallow NVs through implantation with an ion accelerator does not succeed. Plasma immersion ion implantation offers a solution to this problem.

### 3.1.1 Plasma Immersion Ion Implantation (PIII)

PIII is an implantation technique where the substrate is immersed in a plasma of the implantation atoms. Then a high voltage DC pulse accelerates the ions toward the substrate. Even though conventional implantation is more accurate in terms of implantation energy and angle of implantation, PIII utilizes simultaneous implantation and sputtering which leads to a higher quality shallow implanted layer. In this process, damaged layers are constantly being sputtered which makes the higher quality deeper implanted layer closer to the surface.

Typical PIII systems consist of an implantation chamber, a vacuum system, a gas inlet,

a plasma generation mechanism, and an electrode that is connected to a high voltage pulser circuit. For the purpose of this work, we built a compact and highly customizable PIII system.

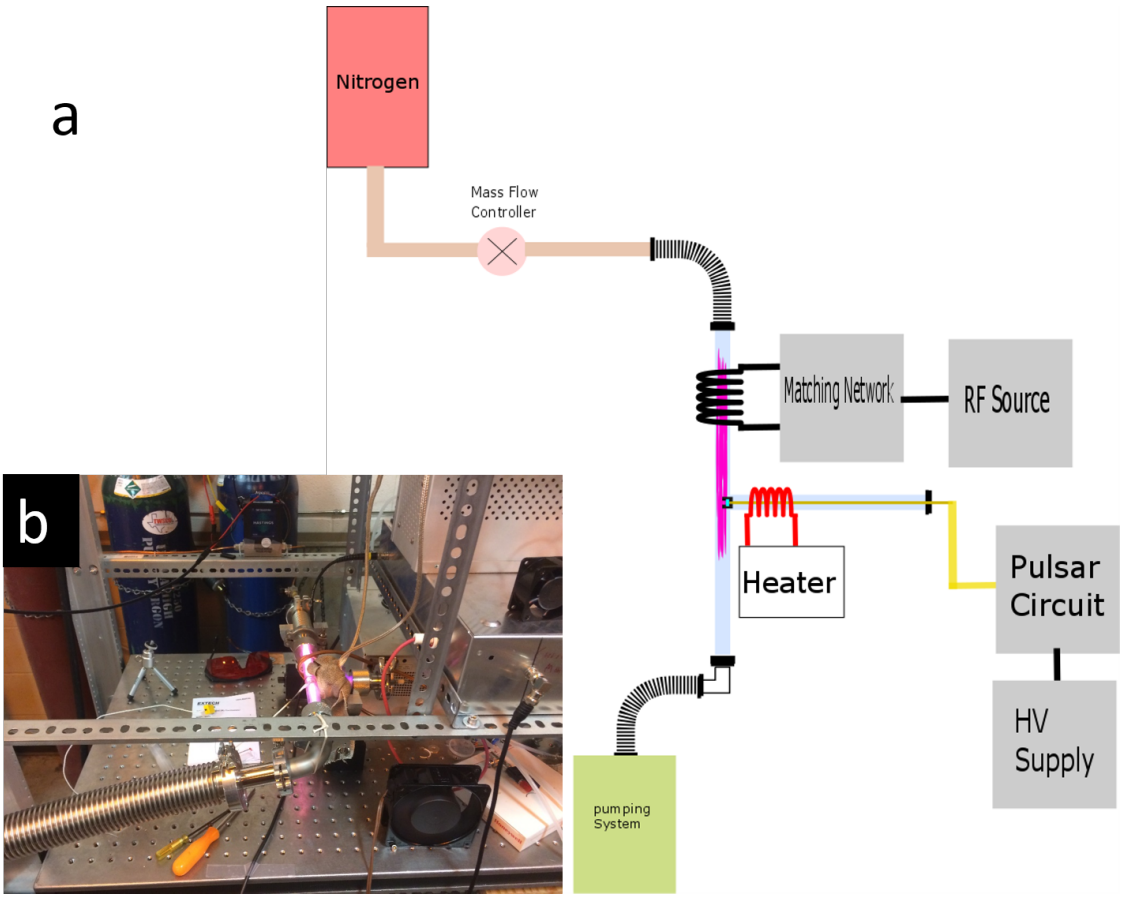


Figure 3.1: a) A diagram showing the parts of our PIII system. b) A photo of our PIII system during implantation.

### *3.1.1.1 Implantation Chamber*

The implantation chamber is a tee shaped quartz tube approximately 1" in diameter. This tube is connected from one side to a vacuum pumping system made of a diffusion

pump and a mechanical pump. The opposite side of the chamber is connected to a nitrogen tank through a 50 SCCM mass flow controller from Hastings HFC-E202-2-50N.

#### *3.1.1.2 Plasma Generation*

In terms of frequency, plasma can be divided into two categories, DC, and RF plasma. RF plasma can be further divided into capacitively coupled and inductively coupled plasma. In DC and capacitively coupled RF plasma, two electrodes are present inside the chamber. The plasma continuously sputters the electrode material contaminating the implantation chamber. On the other hand, inductively coupled plasma uses a coil outside the implantation chamber which makes it suitable for our goal.

In our system, a water-cooled 1/4" copper tube is winded around the quartz tube. The tube was then connected to Advanced Energy's VM1500AW impedance matching network. The network is derived by a 13.56 MHz RF power supply model R301 from Seren.

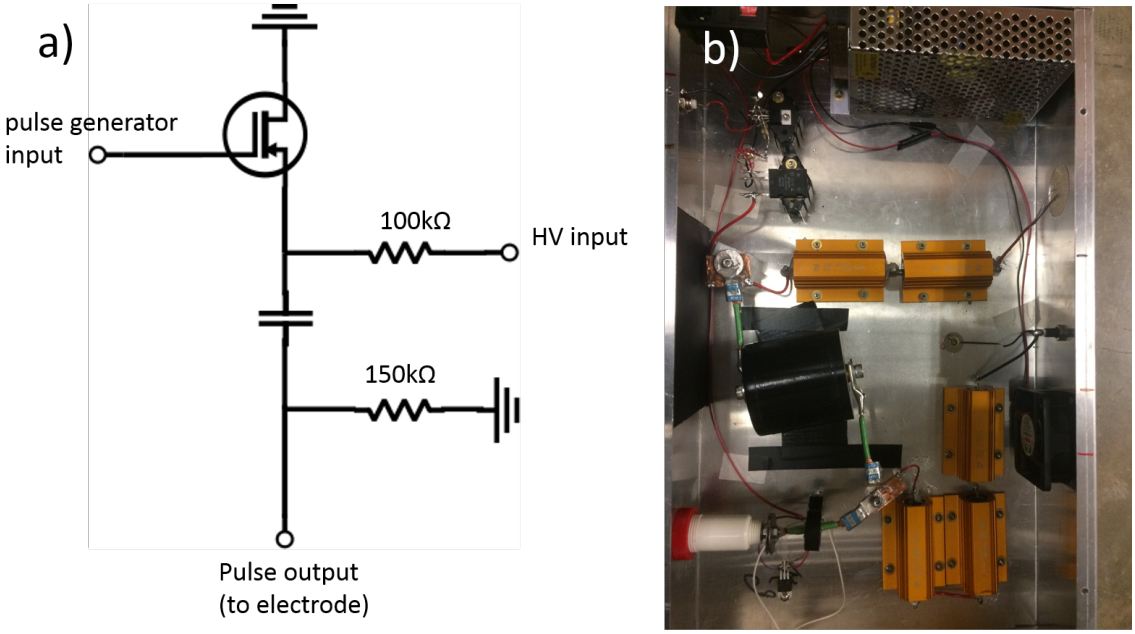


Figure 3.2: a) A diagram of the pulser circuit. b) A photo of our Pulsar circuit.

#### *3.1.1.3 Electrode and Pulsar*

To create an NV layer, the diamond substrate was mounted on the tip of a 1/4" stainless steel electrode and inserted in the chamber. The sides of the electrode were covered by an insulating layer so that implantation only occurred on the tip around the substrate. The electrode was connected to a home built high voltage pulser circuit. Circuit schematics is shown in figure(3.2). We used A 10kV variable power supply from CPS inc. (model 0560) to drive the circuit.

### 3.1.2 Implantation Profile for PIII

In the conventional implantation process, as the accelerated ions penetrate a substrate, they leave a trail of damage. This behavior degrades the quality of the shallow layers of the substrate. This effect is illustrated in figure(3.3). Therefore, conventional implantation fails to create shallow layers of NVs. One way to get around this is to create a deeper layer and then etch the damaged shallow layer. Using this method, an NV 1.9nm deep was engineered successfully [7]. However, the etching process needs to be very precise which caused repeatability issues with this method.

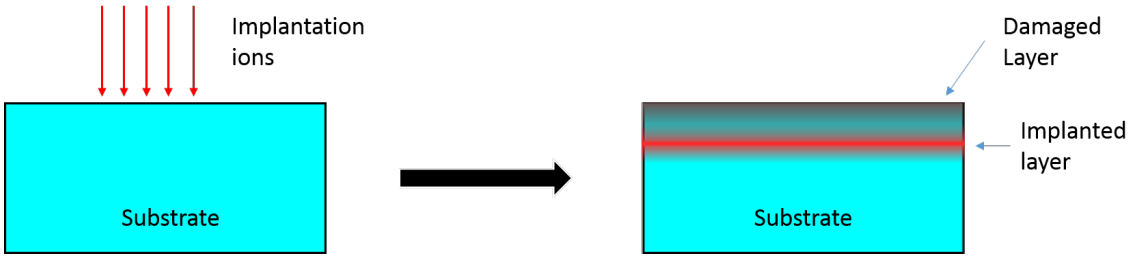


Figure 3.3: An illustration of the damage caused during conventional implantation

PIII implantation techniques overcomes this problem since implantation and etching (sputtering) occurs simultaneously. Figure(3.4) shows the implantation profile for PIII.

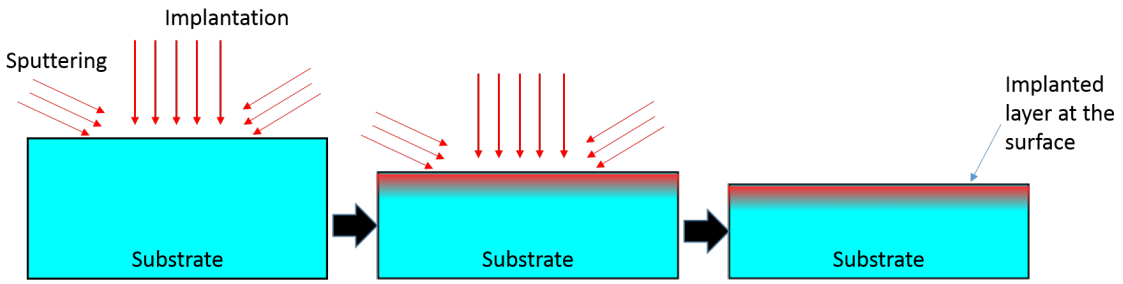


Figure 3.4: implantation profile using PIII. The damaged shallow layer is etched away and a deeper higher quality layer is closer to the surface.

It shows that the damaged layers are continuously sputtered so that the implanted layer maintains a constant distance from the surface. This leads to a higher quality implanted shallow layer. Furthermore, this method does not require high precision. Even if the implanted layer is etched, a new layer will form right below it which makes this technique very consistent.

## 3.2 Shallow NV Growth

Another method of manufacturing diamond crystals with NVs is to introduce nitrogen during the diamond growth. This can be categorized into two major parts: growth of NV layers on top of bulk diamond, or growth of nanodiamonds with NVs. There are two methods for diamond growth: High-Pressure-High-Temperature HPHT, and plasma enhanced chemical vapor deposition CVD. NV layers with depths down to 5nm was demonstrated using CVD growth [15]. As for nanodiamonds, the smallest nanodiamonds that contains negatively charged NVs are 10nm in diameter.

### 3.2.1 Nanodiamond Seeded Growth

The ultimate goal of nanodiamond growth for sensing applications is to manufacture nanodiamonds as small as possible with the highest possible sensitivity. To achieve this goal, the diamond crystal needs to be defects-free, except for the NV itself, and the NV

needs to be as far from the surface as possible, i.e. in the center of the nanodiamond. One growth technique that can do that is seeded growth.

Seeded growth is a crystal growth technique where self-nucleation is not allowed and nucleation only occurs around an organic molecule which is called the seed. Figure(3.5) shows the difference between seeded growth and conventional growth. Basically, there are three main advantages of seeded growth: higher quality crystals, near deterministic defect placement, and the ability to fabricate complex defects.

The threshold of self-nucleation is higher than that of the growth. Therefore, crystals tend to grow rapidly right after nucleation. However, since seeded growth should happen below the self-nucleation threshold, slower growth is possible which is believed to lead to higher quality nanodiamonds.

Also, since the growth process is supposedly isotropic, the seed molecule always end up near the center of the nanodiamond. So if the seed molecule is used to create the color center as well, it will also be near the center of the nanodiamond. For example, if the seed molecule contains one nitrogen atom, then the nanodiamond will have one nitrogen as far as possible from the surface. At this point, vacancies can be created using electron irradiation. Finally, high-temperature annealing leads to the creating of a single NV in the center of the particle.

Finally, since the seed is still a molecule, it can be modified chemically to contain a different number of atoms, or even different isotopes, at specific places in the molecule. This is virtually impossible to do with any other implantation or growth technique.

### 3.2.2 HPHT Growth

In this work, all the HPHT nanodiamond growth took place in Carnegie institution for science. Various equipment were used including multi-anvil cells and diamond anvil cells. Details about equipment and growth procedure can be found elsewhere.

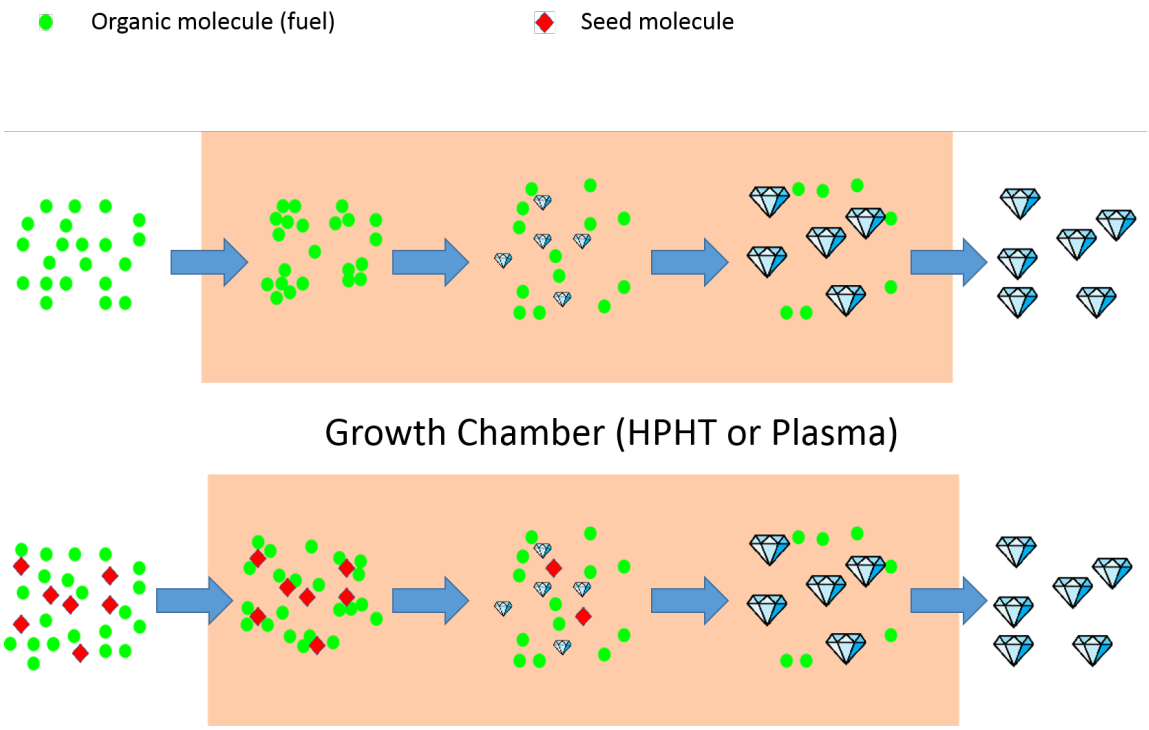


Figure 3.5: Drawing illustrating the difference between conventional growth (above) and seeded (below)

### 3.2.3 Plasma CVD Growth

All the plasma nanodiamonds growth took place in our lab in Texas A&M using a home built microwave plasma system figure(3.6). This system consists of a growth chamber, vacuum pumps, gas inlet, a plasma generation mechanism, and a particle collection mechanism.

The concept of the system is that a carrier gas, most likely argon, runs through a bubbler that contains fuel. In diamond growth experiments, fuel refers to any source of organic molecules that provides the carbon source to grow diamond. After that, the carrier gas mixed with the fuel passes through a region with high microwave power which turns the gas into plasma. The purpose of the plasma is to generate organic radicals. After that,

the gas goes through a high-temperature chamber where nucleation and growth happens. Finally, the growth product is captured downstream with quartz or Teflon filters.

Plasma growth has the advantage that we can introduce different effects and different inputs at different stages of the growth process. So, we designed our growth system with a second gas inlet that does not go through the MW plasma region where we intend to insert seed molecules. The idea is that we want to break the fuel molecules but not seed molecules.

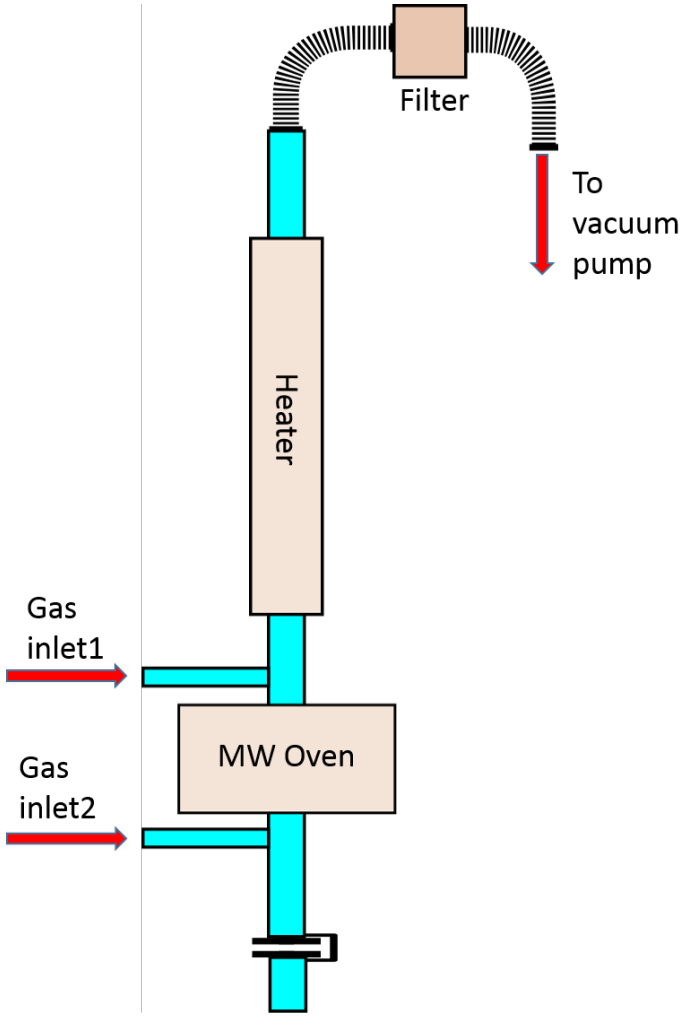


Figure 3.6: Layout of our plasma CVD nanodiamond growth system.

# 4. DIAGNOSTIC TOOLS

## 4.1 Confocal Microscopy

Sensing with NVs requires monitoring of the NV fluorescence, so in order to characterize our NV layers and fluorescent nanodiamonds, we use a home-built confocal microscope. Confocal microscopy is a microscopy technique, where a pinhole is placed in the imaging plane to reject out-of-focus light. In a confocal laser scanning microscope, a 3D image of an object is constructed by scanning it with a laser point-by-point and collecting the fluorescence through the pinhole. Figure(4.1) shows a schematic of the home-built confocal microscope used in this work.

### 4.1.1 Optical Setup

In our microscope, we mainly use 532nm DPSS laser which is sent through a single mode optical fiber. The optical fiber works as a spatial filter to ensure that only TEM00 transverse mode is transmitted which leads to a diffraction limited resolution. The beam, then, is passed through galvo scanner mirrors which are imaged to the back focal plane of the objective lens through a 4f system. In this arrangement, scanning the galvo mirrors translate into scanning the laser spot on the sample. The objective lens is mounted on a piezo stage for Z-scanning. The fluorescence is collected through the same optical path and focused on the pinhole. Finally, the signal is divided with a beam splitter where one half goes to a photon counter and the other goes through grating and focused on a starlight Xpress CCD camera.

The confocal setup was controlled using two national instruments multifunction data acquisition (NiDaq) PCI cards PCI-6259 and PCI-6601. We used these cards to synchronize the movement of the mirrors and the piezo with the photon counter signal in order to create XY, XZ, and YZ scan images. We used a python code to control cards and the rest

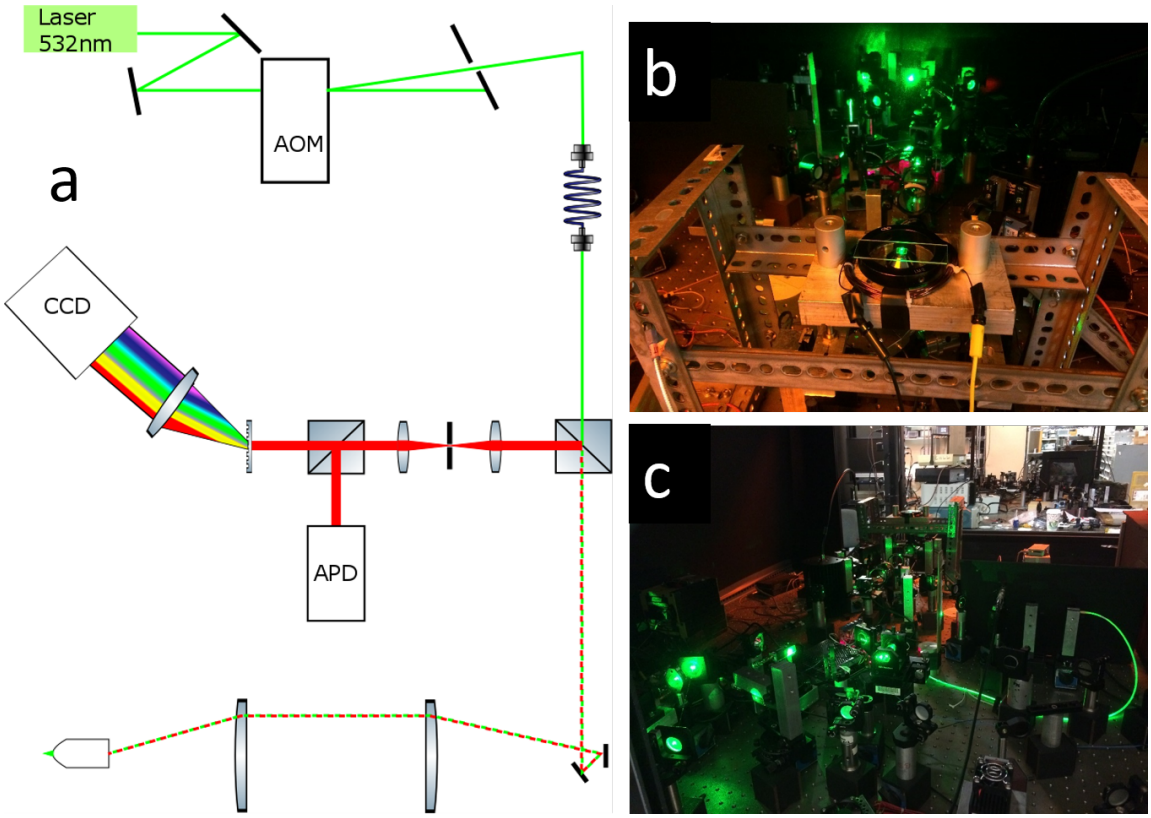


Figure 4.1: a) A diagram showing the parts of our confocal microscope. b and c) photos of the confocal microscope.

of the setup.

National instruments provide a driver software (Ni-Daqmx) which allows users to program their cards using C programming language. We used PyDaqmx which is an open source python package that provides an interface between python and Ni-Daqmx. The control code is too long to be inserted here but we show the graphical interface window with most of the available features in figure(4.2).

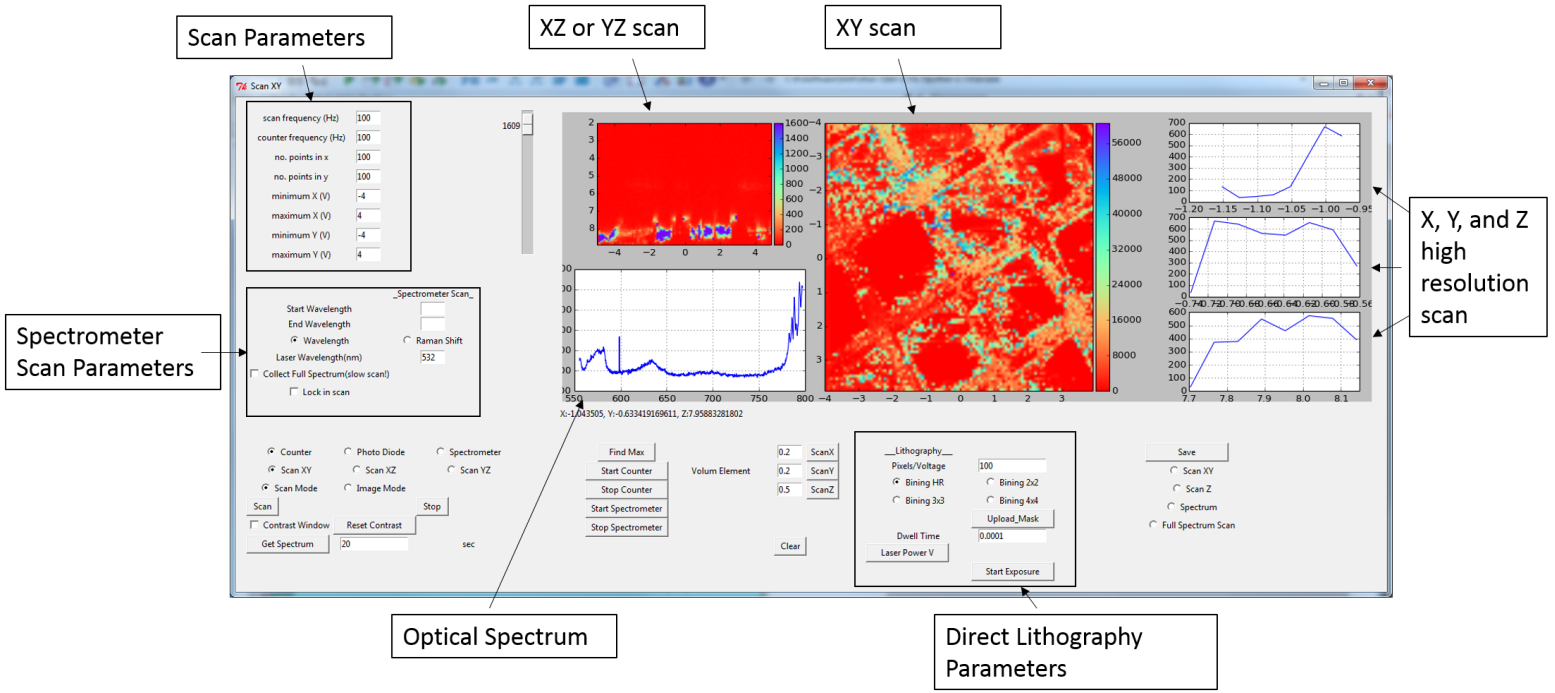


Figure 4.2: Graphical user interface of our confocal control software.

### 4.1.2 Spectrometer

Attaching an optical spectrometer to a confocal microscope allows us to acquire the spectrum of the emission from a diffraction limited spot inside the sample or on its surface. Our spectrometer was simply constructed from two lenses, a transmission grating, and a CCD camera. The signal from the pinhole was imaged onto the CCD chip through a 4f system with the grating placed on the Fourier plane between the two lenses. If aligned correctly, the signal will form a horizontal line on the CCD chip where the pixel number in the horizontal axis depends linearly on the light's wavelength.

For the spectrometer we choose starlight xpress cameras mainly for their low thermal noise. These cameras are equipped with a cooling system that allows for long integration times. However, these cameras have relatively high readout noise, compared to the much more expensive sCMOS cameras, which make them not useful for fast applications or where many images are captured. In this work we used Starlight Xpress SXVR H9.

Straight Xpress provides a dynamic library, namely SxSDK.dll, which allows users to program their cameras using C++. To be able to use the camera as a spectrometer in real time and to integrate it into our confocal software, we wrote a python class that provides an interface to some useful functions in SxSDK.dll as well as useful functions for spectroscopy. We show this python class below.

---

```
import ctypes
from ctypes import byref, POINTER, Structure
from ctypes.wintypes import HANDLE,BYTE
import time
from ctypes import *
import numpy as np
import matplotlib as mpl
```

```
import matplotlib.pyplot as plt

dll = cdll.LoadLibrary("SxSDK.dll")

class params(Structure):
        _fields_ = [('hfront_porch',c_ushort),
        ('hback_porch',c_ushort),
        ('width',c_ushort),
        ('vfront_porch',c_ushort),
        ('vback_porch',c_ushort),
        ('height',c_ushort),
        ('pix_width', c_float),
        ('pix_height', c_float),
        ('color_matrix',c_ushort),
        ('bits_per_pixel',BYTE),
        ('num_serial_ports',BYTE),
        ('extra_caps',BYTE),
        ('vclk_delay',BYTE)]
        def __init__(self):
                pass


class starlight :

        def __init__(self):
```

```
        self.handle = ctypes.c_void_p()
        self.p = params()
        self.camIndex = 0

    def open_camera(self):
        open1 = dll.sxOpen
        open1.resetype = c_int
        open1.argtypes = [HANDLE]
        open1(byref(self.handle))

    def Reset(self):
        Reset = dll.sxReset
        Reset.resetype = c_long
        Reset.argtypes = [HANDLE]
        print Reset(self.handle)

    def Get_Params(self):
        GetCameraParams = dll.sxGetCameraParams
        GetCameraParams.resetype = c_long
        GetCameraParams.argtypes =
            [HANDLE,c_ushort,POINTER(params)]
        GetCameraParams(self.handle, self.camIndex,byref(self.p))

    def Expose(self, time, flags=0, xoffset=0, yoffset=0, width = None,
    height = None, xbin=1, ybin=1):
```

```
        if (width == None):
            width = self.p.width
        if (height == None):
            height = self.p.height
        ExposePixels = dll.sxExposePixels
        ExposePixels.resetype = c_long
        ExposePixels.argtypes =
            [HANDLE,c_ushort,c_ushort,c_ushort,c_ushort,
        c_ushort,c_ushort,c_ushort,c_ushort,c_ulong]
        ExposePixels(self.handle, flags, self.camIndex, xoffset, yoffset,
        width, height, xbin, ybin, time)


def ReadPixels(self,width = None,height = None):
        if (width == None or height == None):
            width = self.p.width
            height = self.p.height
        no_pixels = height * width
        self.Pixels = (c_ushort*no_pixels)()
        ReadPixels = dll.sxReadPixels
        ReadPixels.resetype = c_long
        ReadPixels.argtypes =
            [HANDLE,POINTER(no_pixels*c_ushort),c_ulong]
        ReadPixels(self.handle, byref(self.Pixels), no_pixels)
        image = np.array(self.Pixels[:])
```

```
            return (np.reshape(image,[height,width]))

    def ClearPixels(self,flage=0):
            clear = dll.sxClearPixels
            clear.resetype = c_long
            clear.argtypes = [HANDLE,c_ushort,c_ushort]
            clear(self.handle,flags,self.camIndex)

    def close(self):
            close = dll.sxClose
            close.resetype = c_void_p
            close.argtypes = [HANDLE]
            close(self.handle)


    def calibrate(self,wavelength1,Pix1,wavelength2,Pix2):
            self.a= (wavelength1-wavelength2)/(Pix1-Pix2)
            self.b= wavelength1-self.a*Pix1

    def take_image(self, time, xoffset=0, yoffset=0, width = None, height
        = None, xbin=1, ybin=1):
            if (width == None):
                    width = self.p.width
            if (height == None):
                    height = self.p.height
```

```
        if (ybin == 'height'):
            ybin = height

        self.Expose(time = time, xoffset=xoffset, yoffset=yoffset,
            width = width, height = height, xbin=xbin, ybin=ybin)

        image = self.ReadPixels(width/xbin, height/ybin)

        plt.imshow(image,cmap=mpl.cm.rainbow_r,extent=[int(self.b),
            int(self.a*width+self.b), height/ybin, 0], aspect="auto")
        plt.colorbar()
        plt.show()

    def get_spectrum(self, time, xoffset=0, yoffset=0, width = None,
        height = None, xbin=1, ybin=1):
        if (width == None):
            width = self.p.width
        if (height == None):
            height = self.p.height
        if (ybin == 'height'):
            ybin = height
        self.Expose(time = time, xoffset=xoffset, yoffset=yoffset,
            width = width, height = height, xbin=xbin, ybin=ybin)

        image = self.ReadPixels(width/xbin, height/ybin)
```

```
        I = np.sum(image, axis=0)
        Wavelength= self.a*np.array(range(width))+self.b
        return Wavelength,I

    def get_intinsity(self, time, wavelength1, wavelength2, yoffset = 0,
        height = None, xbin=1, ybin=1):
        pix1 = int((wavelength1-self.b)/self.a)
        pix2 = int((wavelength2-self.b)/self.a)

        xoffset = pix1
        width = pix2 - pix1
        if (xbin == 'width'):
            xbin = width
        if (ybin == 'height'):
            ybin = height
        if (height == None):
            height = self.p.height
        self.Expose(time = time, xoffset=xoffset, yoffset=yoffset,
            width = width, height = height, xbin=xbin, ybin=ybin)

        image = self.ReadPixels(width/xbin,height/ybin)
        I = np.sum(image)
        if (I > 65500):
            print "WARNING: SATURATION"
        return (I)
```

### 4.1.3 MW Excitation Setup

Most sensing protocols using NVs utilizes MW signal to drive the NVs spin transitions. Therefore, the microscopes sample holder was modified to accommodate PCB boards which deliver the MW signal to the diamond. These PCB boards have very simple designs and they were manufactured by us using laser printers and a PCB Fab-in-a-Box kit. A typical sample holder for most experiments in this work is shown in figure(4.4).

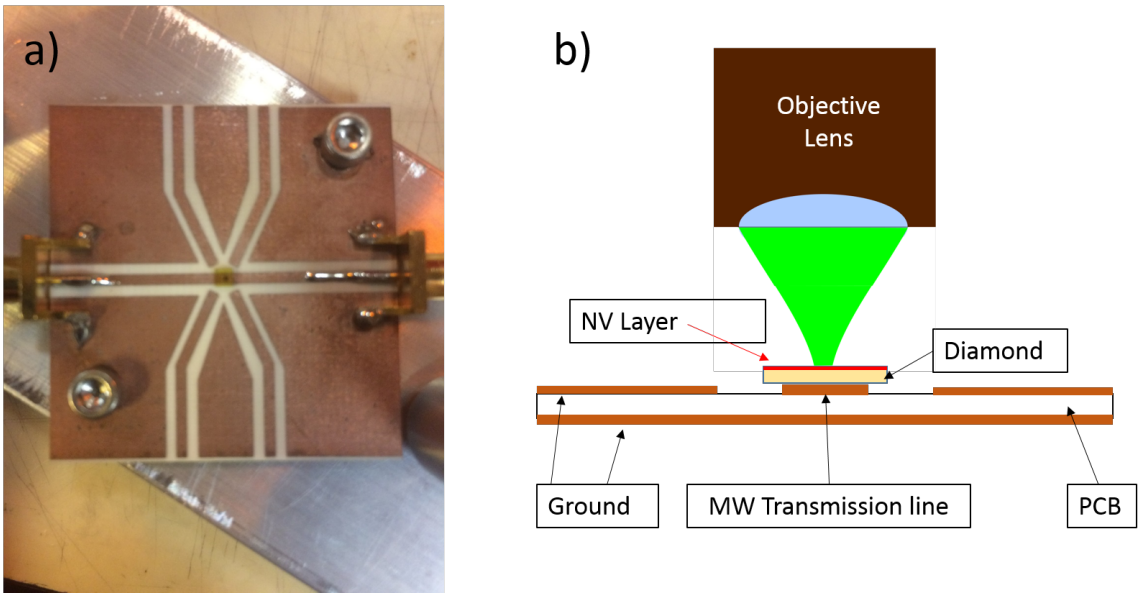


Figure 4.3: Typical design of PCB boards used in this work.

The MW setup is shown in figure(4.5). The MW signal is generated using ADF4351 evaluation board. The signal was sent through two MW amplifiers and then to the PCB board where the sample is mounted. Finally, the signal is terminated at a spectrum analyzer where we monitor the MW frequency and power. Again we wrote a python code to synchronize the MW setup with the photo detection in order to generate ODMR spectrums among other things. This code is too long to include here, but we show the graphical

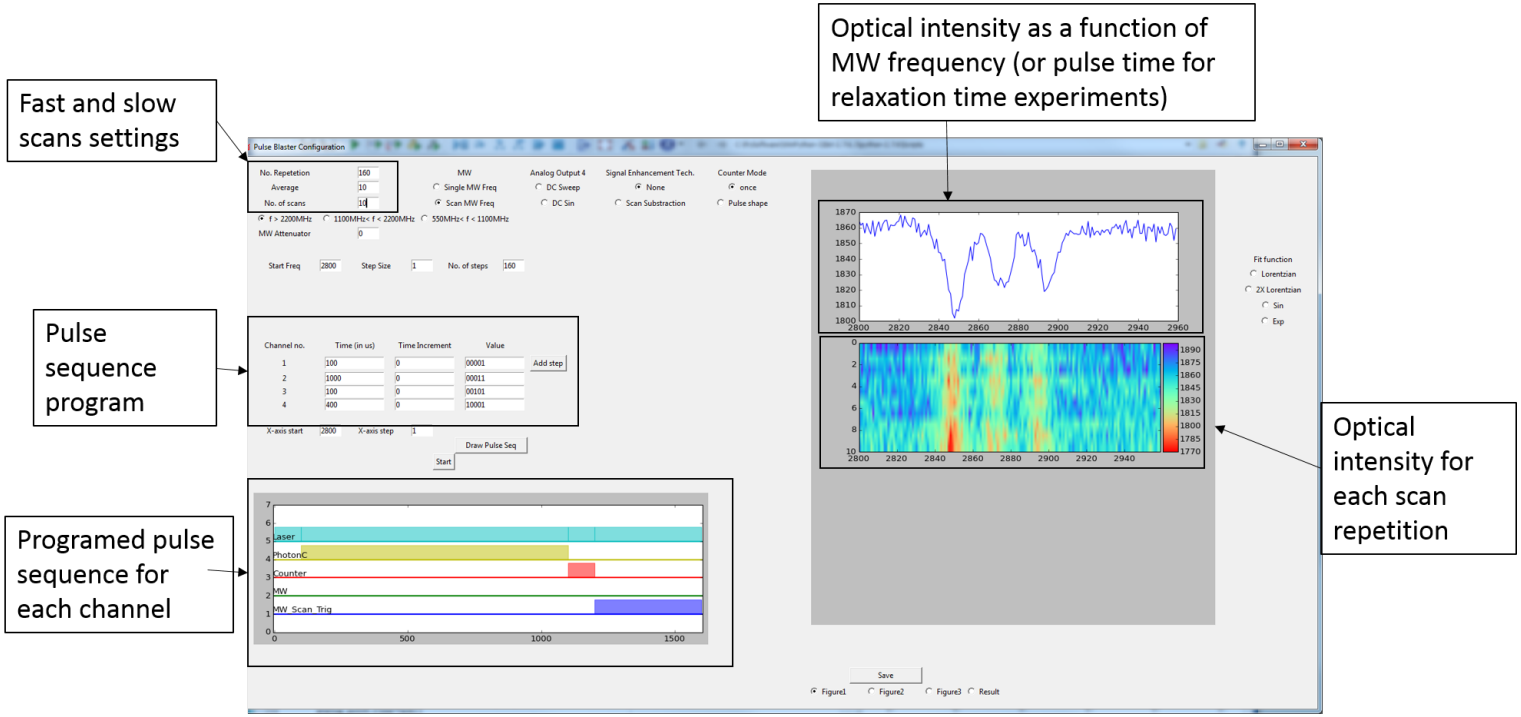


Figure 4.4: Graphical user interface of our MW control software.

interface highlighting some of the code's features in figure(4.4).

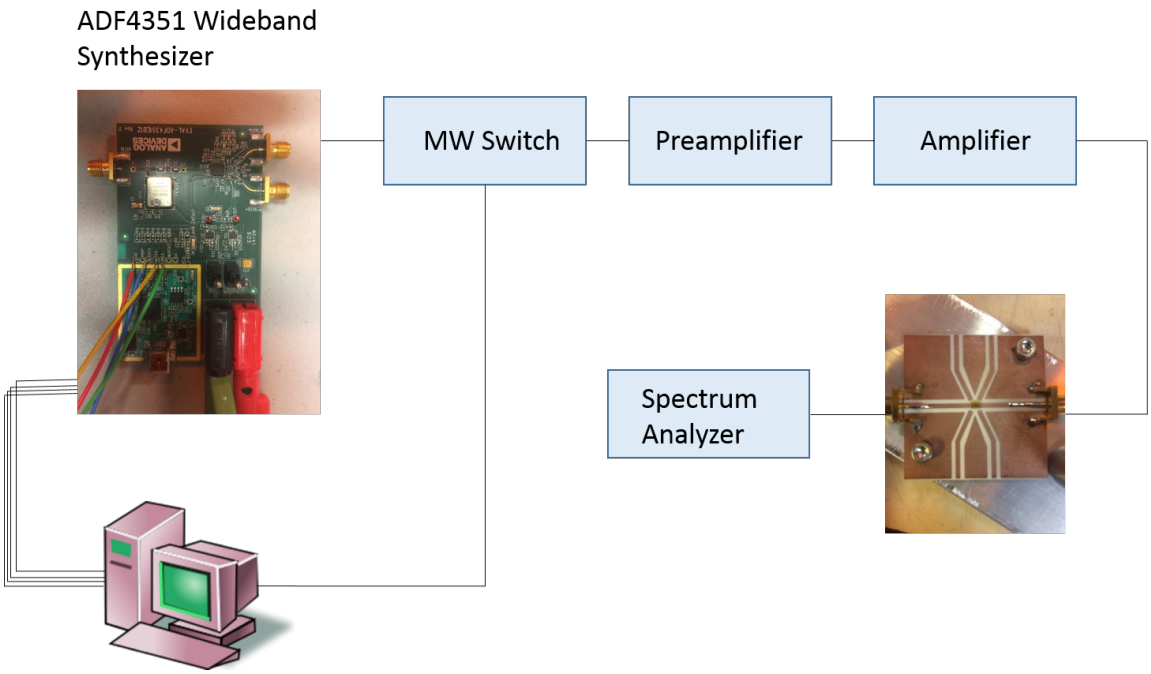


Figure 4.5: a) A diagram showing the MW system

The ADF4351 board was wired directly to the NiDaq card PCI-6259 bypassing the USB controller so that MW frequency scanning is synchronized with different functions of the microscope. This also allows for fast frequency scans with sub-millisecond dwell time. Fast frequency scaning is a good technique to overcome low-frequency noise. We wired four digital channels from the NiDaq to the ADF4351 board. The digital channels are Chip Enable (CE), Load Enable (LE), data, and clock. Then we wrote the python class shown below to control the board through these four channels.

---

```
from PyDAQmx import Task
import  numpy as np
```

```
import time
from fractions import Fraction

class ADF4351:

    def __init__(self):

        self.clk=10000000.0
        self.write = int32()
        self.read = int32()
        self.d_read = int32()

        self. register0 = np.zeros(32,dtype=np.uint8)
        self. register1 = np.zeros(32,dtype=np.uint8)
        self. register2 = np.zeros(32,dtype=np.uint8)
        self. register3 = np.zeros(32,dtype=np.uint8)
        self. register4 = np.zeros(32,dtype=np.uint8)
        self. register5 = np.zeros(32,dtype=np.uint8)


    def initiate_board(self,FreqRange=1):

        Chip_enable=Task()
        Chip_enable.CreateDOChan("Dev1/port0/line7","",
        DAQmx_Val_ChanForAllLines)
```

```
Chip_enable.CfgSampClkTiming("100kHzTimebase",100000,
DAQmx_Val_Rising,DAQmx_Val_FiniteSamps,2)
Chip_enable. WriteDigitalLines  (2,0,100.,
DAQmx_Val_GroupByScanNumber,np.array([1,1],dtype=np.uint8),
byref( self . write ) ,None)
Chip_enable. StartTask ()
Chip_enable.WaitUntilTaskDone(-1)
Chip_enable.ClearTask()


w0 = np. array ( list (bin(0x320000)))
w0 = w0[2:]. astype(np. uint8 )
 self .  register0 [-np.size(w0):]  = w0

w1 = np. array ( list (bin(0x8008011)))
w1 = w1[2:]. astype(np. uint8 )
 self .  register1 [-np.size(w1):]  = w1

w2 = np. array ( list (bin(0x4E42)))
w2 = w2[2:]. astype(np. uint8 )
 self .  register2 [-np.size(w2):]  = w2

w3 = np. array ( list (bin(0x4B3)))
w3 = w3[2:]. astype(np. uint8 )
 self .  register3 [-np.size(w3):]  = w3
```

```
if  (FreqRange == 1):
            w4 = np.array( list (bin(0x8C803C)))
             self .f_pdf  = 25.0
elif (FreqRange == 2):
            w4 = np.array( list (bin(0x9C803C)))
             self .f_pdf  = 12.5
w4 = w4[2:].astype(np.uint8)
self . register4 [-np.size(w4):] = w4
self . register4 [-5]=0

w5 = np.array( list (bin(0x580005)))
w5 = w5[2:].astype(np.uint8)
self . register5 [-np.size(w5):] = w5


self . register  =
    np.array([ self . register5 , self . register4 , self . register3 ,
self . register2 , self . register1 , self . register0 ])

for  i  in  range(6):
            Data = np.append( self . register [i ],[0])
            no_samples = np.size(Data)

            LE = np.zeros(np.size(Data),dtype = np.uint8)
```

```
LE[-1:] = 1

clk_out = Task()
clk_out.CreateCOPulseChanFreq("Dev1/ctr1","",
DAQmx_Val_Hz,DAQmx_Val_Low,0,self.clk,0.5)
clk_out.CfgImplicitTiming(DAQmx_Val_FiniteSamps,
    no_samples)

Digital_Output = Task()
Digital_Output.CreateDOChan("Dev1/port0/line0:1","",
DAQmx_Val_ChanPerLine)
Digital_Output.CfgSampClkTiming("Ctr1InternalOutput",
self.clk,DAQmx_Val_Falling,DAQmx_Val_FiniteSamps,
no_samples)
Digital_Output.WriteDigitalLines(no_samples,0,100.,
DAQmx_Val_GroupByChannel,np.array(([Data],[LE]),
dtype=np.uint8),byref(self.write),None)

Digital_Output.StartTask()
clk_out.StartTask()

Digital_Output.WaitUntilTaskDone(-1)

Digital_Output.ClearTask()
clk_out.ClearTask()
```

```
def setFreq(self, freq):

        N = int(freq / self.f_pdf)
        r = freq / self.f_pdf - N
        Mod = Fraction(r).denominator
        if (Mod > 4095):
                Mod = 4095
        elif (Mod < 2):
                Mod = 2
        frac = int(r*Mod)

        self.register0[-(12+3):-3] = np.zeros(12)
        B_frac = np.array(list(bin(frac)))
        B_frac = B_frac[2:].astype(np.uint8)
        self.register0[-(np.size(B_frac)+3):-3] = B_frac

        self.register0[-(16+15):-15] = np.zeros(16)
        B_N = np.array(list(bin(N)))
        B_N = B_N[2:].astype(np.uint8)
        self.register0[-(np.size(B_N)+15):-15] = B_N

        self.register1[-(12+3):-3] = np.zeros(12)
        B_Mod = np.array(list(bin(Mod)))
        B_Mod = B_Mod[2:].astype(np.uint8)
```

```
self . register1 [-(np.size(B_Mod)+3):-3] = B_Mod

Data = np.hstack((self.register1,[0], self.register0,[0]))
LE = np.hstack((np.zeros(np.size(self.register1),dtype =
    np.uint8),[1], np.zeros(np.size(self.register0),dtype =
    np.uint8),[1]))

no_samples = np.size(Data)

clk_out = Task()
clk_out.CreateCOPulseChanFreq("Dev1/ctr1","",DAQmx_Val_Hz,
DAQmx_Val_Low,0,self.clk,0.5)
clk_out.CfgImplicitTiming(DAQmx_Val_FiniteSamps, no_samples)

Digital_Output = Task()
Digital_Output.CreateDOChan("Dev1/port0/line0:1","",
DAQmx_Val_ChanPerLine)
Digital_Output.CfgSampClkTiming("Ctr1InternalOutput",self.clk,
DAQmx_Val_Falling,DAQmx_Val_FiniteSamps,no_samples)
Digital_Output.WriteDigitalLines(no_samples,0,100.,
DAQmx_Val_GroupByChannel,
np.array(([Data],[LE]),dtype=np.uint8),byref(self.write),None)

Digital_Output.StartTask()
clk_out.StartTask()
```

```
                Digital_Output.WaitUntilTaskDone(-1)

                clk_out.ClearTask()
                Digital_Output.ClearTask()

def scanFreq(self, startFreq, stepSize, no_steps, repeats=1):
                # All frequency units are MHz

                Data = np.array([], dtype=np.uint8)
                LE = np.array([], dtype=np.uint8)
                for i in range(no_steps):
                                freq = startFreq + i * stepSize

                                N = int(freq / self.f_pdf)
                                r = freq / self.f_pdf - N
                                Mod = Fraction(r).denominator
                                if (Mod > 4095):
                                                Mod = 4095
                                elif (Mod < 2):
                                                Mod = 2
                                frac = int(r*Mod)

                                self.register0[-(12+3):-3] = np.zeros(12)
                                B_frac = np.array(list(bin(frac)))
```

```
                B_frac = B_frac[2:].astype(np.uint8)
                self.register0[-(np.size(B_frac)+3):-3] = B_frac

                self.register0[-(16+15):-15] = np.zeros(16)
                B_N = np.array(list(bin(N)))
                B_N = B_N[2:].astype(np.uint8)
                self.register0[-(np.size(B_N)+15):-15] = B_N

                self.register1[-(12+3):-3] = np.zeros(12)
                B_Mod = np.array(list(bin(Mod)))
                B_Mod = B_Mod[2:].astype(np.uint8)
                self.register1[-(np.size(B_Mod)+3):-3] = B_Mod

                Data = np.hstack((Data, self.register1,[0],
                self.register0,[0]))
                LE = np.hstack((LE,
                np.zeros(np.size(self.register1),dtype = np.uint8),[1],
                np.zeros(np.size(self.register0),dtype =
                    np.uint8),[1]))

        Data = np.tile(Data, repeats)
        LE = np.tile(LE,repeats)

        no_samples = np.size(Data)
```

```
clk_out = Task()
clk_out.CreateCOPulseChanFreq("Dev1/ctr1","",DAQmx_Val_Hz,
DAQmx_Val_Low,0,self.clk,0.5)
clk_out.CfgImplicitTiming(DAQmx_Val_FiniteSamps,
    int(no_samples/no_steps/repeats))
clk_out.CfgDigEdgeStartTrig("PFI4",DAQmx_Val_Rising)
clk_out.SetStartTrigRetriggerable(1)

Digital_Output = Task()
Digital_Output.CreateDOChan("Dev1/port0/line0:1","",
DAQmx_Val_ChanPerLine)
Digital_Output.CfgSampClkTiming("Ctr1InternalOutput",self.clk,
DAQmx_Val_Falling,DAQmx_Val_FiniteSamps,no_samples)
Digital_Output.WriteDigitalLines(no_samples,
0,100.,DAQmx_Val_GroupByChannel,
np.array(([Data],[LE]),dtype=np.uint8),byref(self.write),None)

Digital_Output.StartTask()
clk_out.StartTask()
Digital_Output.WaitUntilTaskDone(-1)
clk_out.ClearTask()
Digital_Output.ClearTask()
```

### 4.1.4 SNR Enhancement

For any sensor, the best sensitivity is obtained when all classical noise is suppressed. In our microscope, low-frequency noise in laser intensity or from mechanical vibration degrades the sensitivity of the measurement. To overcome this problem, we modulate the MW field then, the collected signal from the photon counter is demodulated in software. This can be considered as a digital form of lock-in-amplifier SNR enhancement. Figure(4.6) shows the same ODMR spectrum generated with continuous MW and modulated MW.

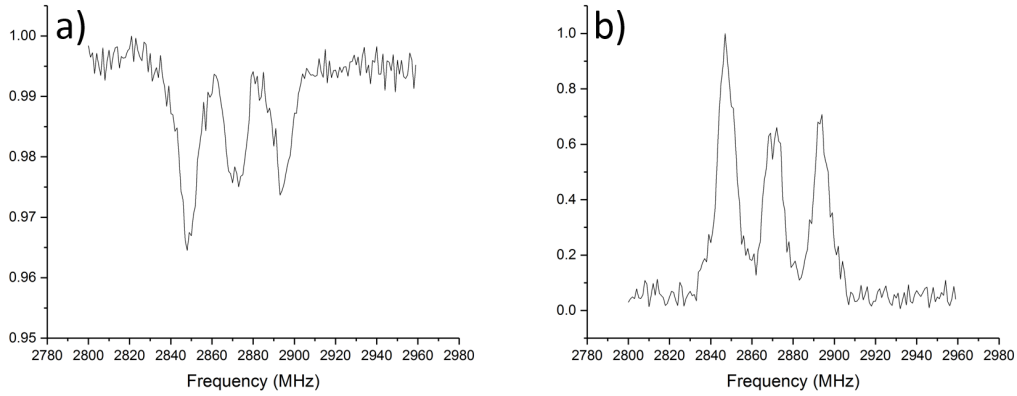


Figure 4.6: The same ODMR spectrum generated using a)CW MW, and b)modulated MW signal

## 4.2 Transmission Electron Microscopy (TEM)

TEM is an electron microscopy technique where a collimated electron beam is sent through a thin sample and then scattered electrons are imaged onto a screen or a camera. Similar to most electron beam microscopy techniques, TEM typically achieves sub-nanometer resolution. In this work, TEM was used for imaging nanoparticles, recognize

nanodiamonds by studying electron diffraction patterns, and create vacancies in nanodiamond using electron irradiation. All data shown here are generated using JOEL2010 TEM system in the Microscopy and Imaging Center (MIC) at Texas A&M University.

Electron microscopy is usually the first tool we use to analyze the outcome of growth experiments. After any growth experiment, the product is loaded into a TEM grid and inserted into the microscope. The first step is to locate the particles under the microscope. Sometimes high-temperature annealing around 700C in vacuum for a few minutes is required to evaporate any material that might be covering the nanoparticles. Once the particles are found, we use electron diffraction patterns to identify the type of particles.

### 4.2.1 Electron Diffraction Pattern

When an electron beam is scattered through a crystal, the path difference between electrons scattered from two parallel crystal plan is $2dsin\theta$, where d is the interplenary distance and $\theta$ is the scattering angle. We get constructive interference when the path difference is equal to an integer multiple of the electron's wave length. Scattering angles that satisfy this condition are called Bragg angles and they satisfy the famous Bragg equation:

$$n\lambda = 2dsin\theta_B \tag{4.1}$$

The set of angles that satisfies equation (4.1) can be directly readout from the diffraction pattern. The distance d is directly related to the lattice symmetry and the lattice constants. For example, for a cubic lattice with lattice constant $a$, the interplenary distance d equals:

$$d = \frac{a}{\sqrt{h^2 + k^2 + l^2}} \tag{4.2}$$

Where h,k ,and l are Miller indices. The intensity of different diffraction beams are not

the same. Therefore, for each type of crystal, there are one or two scattering angles that are much brighter than the rest. All this give unique diffraction patterns for different types of crystals.

Cubic diamond has a face-centered cubic lattice with lattice constant a =3.567 A. Each primitive cell contains 2 carbon atoms at positions (0,0,0) and (1/4,1/4,1/4). The brightest diffraction occurs from the <111> planes which corresponds to d = a/sqrt(3) = 2.05 A.

### 4.2.2 Electron Irradiation

In this work, we used electron irradiation to create vacancies in the diamond lattice. Then, high-temperature annealing diffuses these vacancies in the diamond lattice until they are trapped by a substitutional nitrogen and the NV center is formed. To create a vacancy, the energy transferred from an incident projectile to the target particle needs to exceed a minimum value called the displacement energy threshold.

The energy transferred TE from an incident particle with mass m to a substrate particle of mass M is given by:

$$T_E = E_0 \frac{4mM}{(m+M)^2} sin^2(\frac{\theta}{2}) \tag{4.3}$$

Where:

$E_0$ = is the energy of the incedent particle

$\theta$ = is the scattring angle

For electron irradiation of a diamond substrate with a 200kev electrons, the transferred energy is:

$$T_E \approx 36.5eV \times sin^2(\frac{\theta}{2}) \tag{4.4}$$

The displacment energy threshold of diamond was measured to be $35 \pm 5eV$ [16].

# 5. SHALLOW LAYERS IN BULK CRYSTALS

## 5.1 Choice of Diamond Substrate

As discussed earlier, negatively charged NV is not stable near the surface due to electron traps on and near the diamond surface. To stabilize the NVs charge state, the diamond lattice needs to contain electron donors (n-doped) like nitrogen or phosphorous. While doping diamond with phosphorous is technically advanced, nitrogen doped (type Ib) diamond is available in great quantities and very low prices. Therefore, all shallow implantations in this work were performed on type Ib diamond plates acquired from (Element 6) and (Sumitomo).

## 5.2 Shallow Implantation

A type 1b high-pressure-high-temperature (HPHT) diamond from element six was loaded on the stainless steel electrode and inserted in our PIII chamber. Then, the chamber was sealed and pumped to high vacuum. Then, a flow of a 50 SCCM of Nitrogen was sent through the chamber through the MFC at the inlet. 200Watts of RF power was sent through the coil (Figure3.1) to generate Nitrogen plasma. We used our home-built pulser circuit to generate implantation pulses at 4kV with repetition rate of 250Hz and duty cycle $10\%$. The implantation was performed at room temperature.

After the implantation, the diamond was inspected with the confocal microscope, but no NVs were found. This is expected since the implantation would lead to substitutional nitrogen and vacancies but not necessarily NVs. Then, the diamond was annealed under high vacuum at 890C for 2.75 hours. The annealing process diffuses the vacancies in the diamond crystal until they are trapped by a substitutional nitrogen creating the NV center. After annealing, a bright layer of NVs was detected using the confocal microscope (figure5.1).

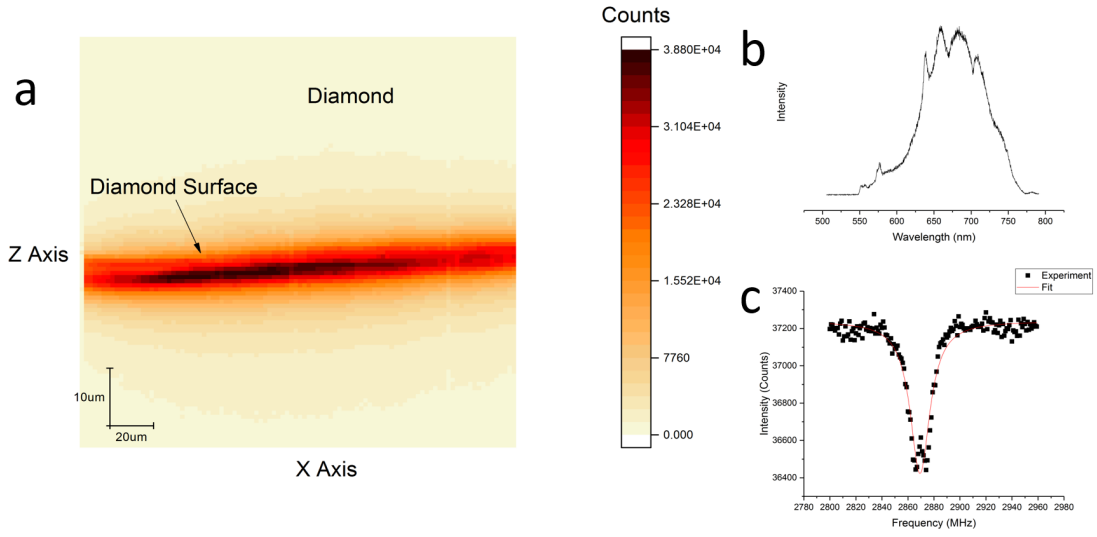


Figure 5.1: a) An XZ confocal scan showing a bright layer of NVs in the implanted diamond surface. Thickness of the layer is below the resolution limit of the confocal microscope. b) Optical spectrum of the implanted layer. C) An ODMR spectrum of the implanted layer.

## 5.3 High-temperature Implantation

A similar implantation procedure was repeated except that the chamber's temperature around the sample was elevated to more than 800C. For high-temperature implantation, NV layers are created without the post-annealing step. However, for some of our samples, post-annealing improved the brightness of the NV layer.

More importantly, high-temperature implantation improves the quality of the NV layer significantly. Figure(5.2) shows the ODMR spectrum for two identical type Ib diamonds from Sumitomo for layers that were implanted at room temperature and at high temperature. The high-temperature implantation increased the contrast of the ODMR peak and reduced its width which improves the magnetic sensitivity.

When implanting at high temperatures, vacancies created during the implantation are constantly diffusing. This prevents the accumulation of very stable long vacancies chains.

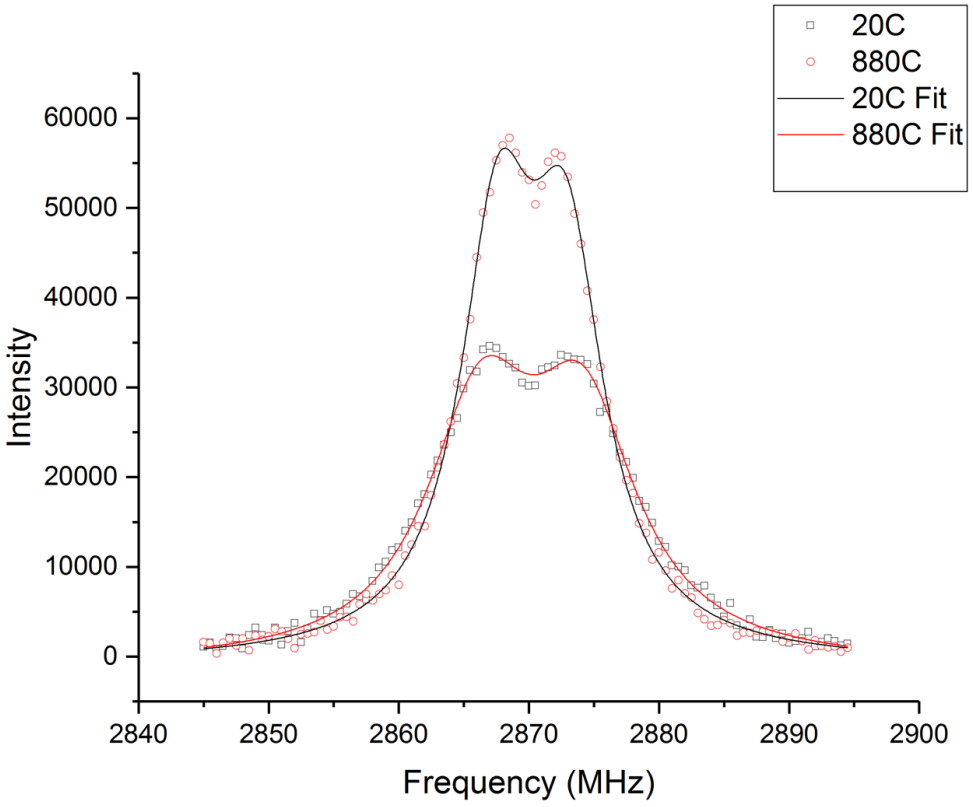


Figure 5.2: Comparison between ODMR spectra of shallow NV layer implanted in room temperature (black) and in 880C (red).

Those chains have a binding energy stronger than that of the NV which means curing them will require annealing at temperatures above 1200C where the NVs will disappear. Furthermore, some of these vacancy chains are paramagnetic, so they introduce significant magnetic noise. This noise broadens the ODMR spectrum of the NVs ensemble lowering their magnetic sensitivity.

### 5.4 Red Excitation and Biocompatibility

Another advantage of using n-doped diamond is that it allows NVs to be optically excited with red lasers instead of green. In intrinsic diamond, red laser depletes the charge

of the NV turning it to $NV_0$. For the NV to regain its charge, first it needs to get optically excited. While green photons can excite $NV_0$s, red photons cannot. This process is very well explained here [17]. The advantage of red excitation over green is mainly for bio-sensing applications. Photo-toxicity of green light is orders of magnitudes higher than that of red light[18]. Figure(5.3) shows an ODMR spectrum generated by using a 636nm excitation from one of our shallow layers.

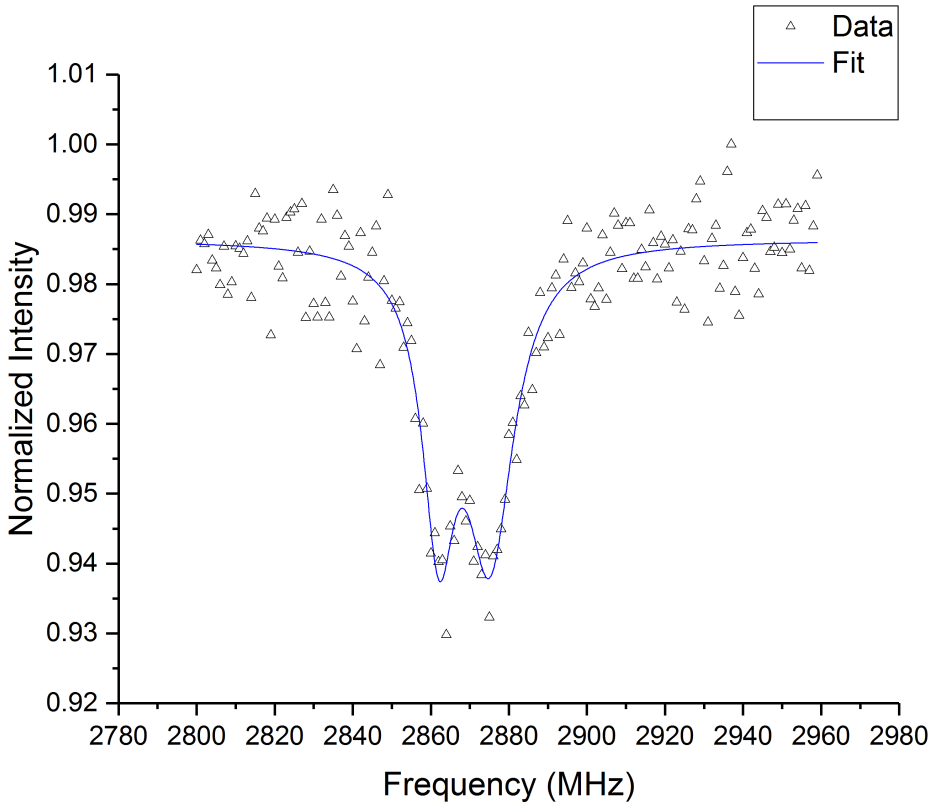


Figure 5.3: AN ODMR spectrum of one of our shallow implanted layers where the NVs were excited using 636nm laser.

## 5.5 Layer Depth Estimation Using FRET

Since the depth and thickness of our shallow NV layers are well beyond the resolution limit of the confocal microscope, we need a different method to estimate the layers' depth and thickness. One simple way to estimate the depth is to utilize a near-field phenomenon known as Forster Resonance Energy Transfer (FRET).

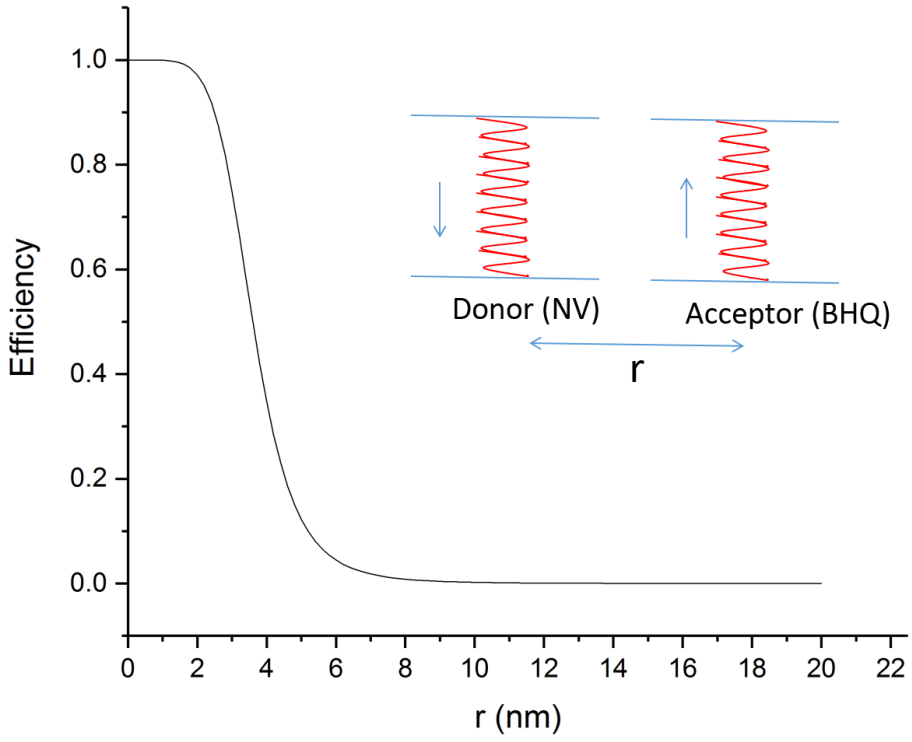


Figure 5.4: FRET Efficiency between NV and BHQ3 vs distance

It is well known that the radiation intensity of an oscillating electrical dipole decays as $1/r^2$ in the far field. However, when there is an absorber in the near field $\lambda >> r$ of

the oscillating dipole (emitter) with the same resonance frequency, then the energy will transfer non-radiatively from the emitter to the absorber. This effect can be measured by monitoring the fluorescence of the donor which gets quenched significantly as the absorber gets close to it. The fret efficiency is given by:

$$E = \frac{R_0^6}{R_0^6 + r^6} \tag{5.1}$$

$R_0$ is the fret radius which equals to

$$R_0 = 0.211(\kappa^2 n^{-4} Q_D j(\lambda))^{1/6} \tag{5.2}$$

Where

$\kappa$ = is the orientation factor, for average orientation $\kappa^2 = 2/3$

n = is the medium's refractive index

$Q_D$ = is the quantum efficiency

j($\lambda$) = is the spectral overlap between the emission spectrum of the emitter and the absorption spectrum of the acceptor

Notice that the fret efficiency is a sharply decaying function at $R_0$ So the fluorescence of any emitter closer than $R_0$ to an absorber will quench effectively and emitters further than $R_0$ will not be affected.

It has been shown that the NV fluorescence is quenched when it is placed in the vicinity of a Black-Hole-quencher 3 (BHQ3). BHQs are a type of organic molecules that absorb optical photons and relax non-radiatively.The fret radius between the NV and the BHQ3 molecule was calculated to be 3.6nm [19]. We use this concept to show that most of the NVs in our engineered shallow layers are closer than 3.6nm to the diamond's surface. Figure (5.4) shows the quenching efficiency of the NV fluorescence as a function of the distance between NVs and BHQ3 molecules on the diamond surface.

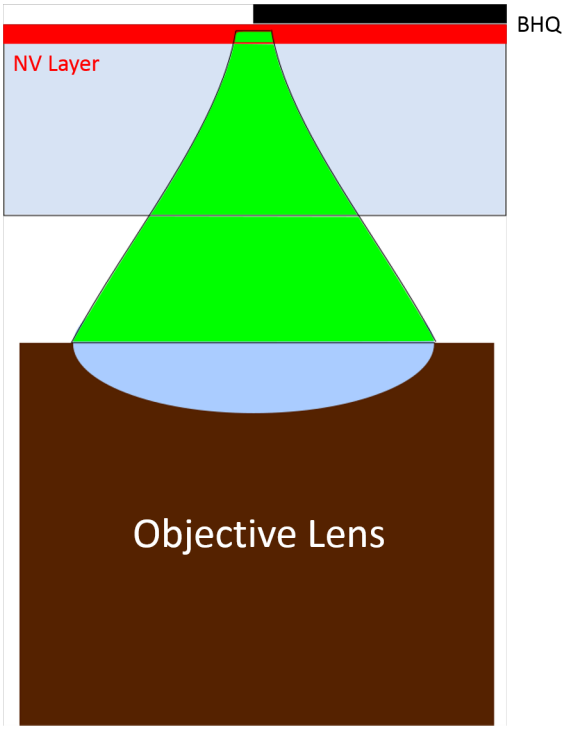


Figure 5.5: Illustration of FRET experiment where we covered half of the diamond's surface with a layer of BHQ3

To carry out this experiment, we masked half of the diamond surface, then we put a drop of BHQ3 suspended in ethanol and left it to dry. After that, the mask was removed and so half the surface was covered with BHQ3, whereas the rest was not. Then, using a confocal microscope, we illuminate the NV layer through the diamond so that the BHQ3 layer does not block the laser figure(5.5). In figure(5.6) We show clearly that the NVs' fluorescence was quenched effectively by BHQ3 which proves most of the NVs are indeed within the FRET radius.

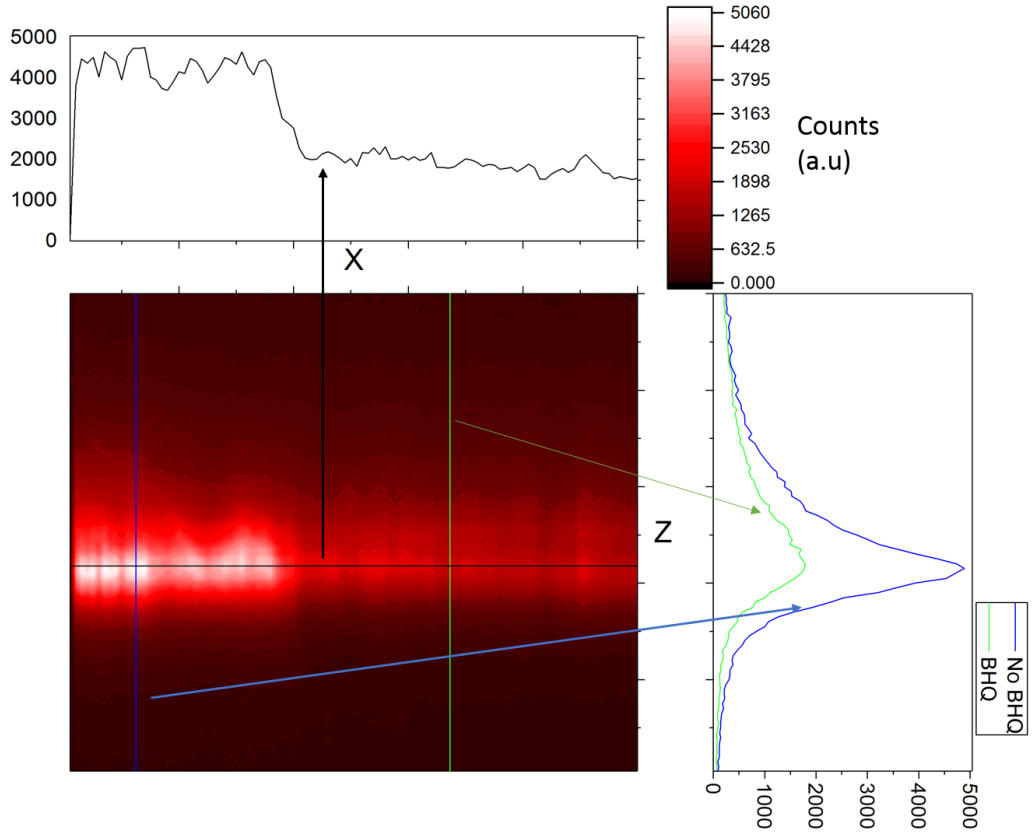


Figure 5.6: XZ confocal scan to one of our shallow NV layers in the configuration shown in figure(5.5). Fluorescence of NVs below the BHQ3 layer was quenched effectively which means most of the NVs are within the FRET radius.

## 5.6 Characterization of the Layer's Sensitivity

To estimate the layer's performance for different applications, it is necessary to know the depth, thickness, and NV density of the layer. From the FRET results, we can estimate the layer's depth and thickness to be 2nm and 3nm respectively. We can also, estimate the NV density since we get approximately 100NV per the laser spot size. This gives us a density of around 2.7 ppm.

Figure(5.7) shows magnetic sensitivity measurement for one of our layers. In this experiment, the microwave frequency we set to 2860 MHz and was modulated at 1 kHz

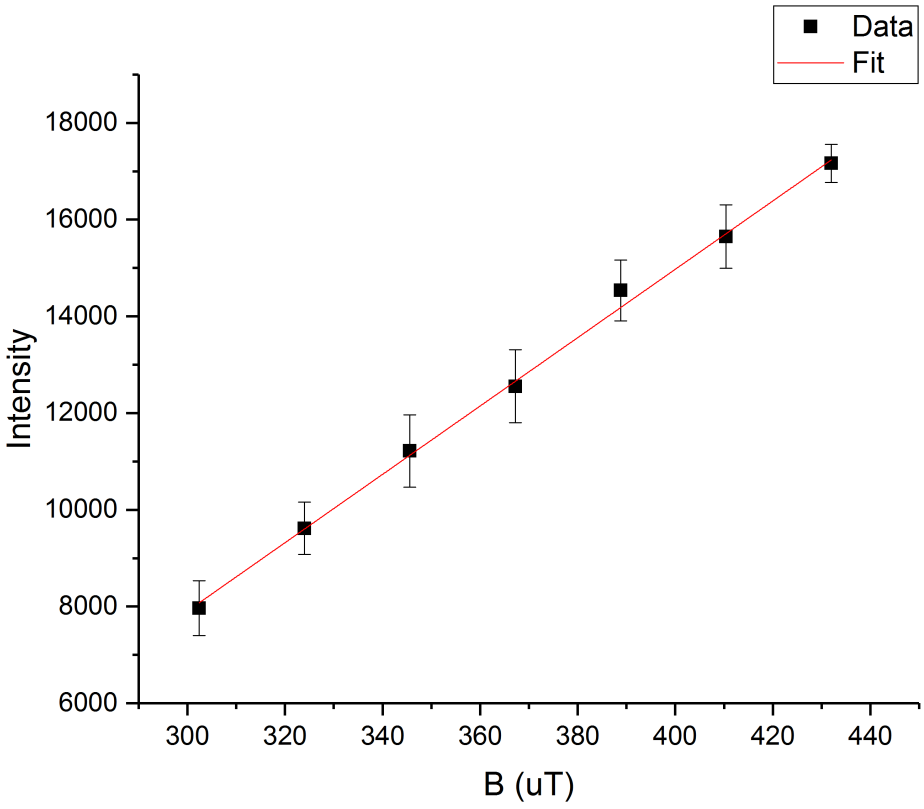


Figure 5.7: Magnetic sensitivity measurement of one of our NV shallow layers. A DC magnetic field was scanned while monitoring the NVs' fluorescence. Each measurement was repeated 10 times and the error bar represents the standard deviation of the measurements. The MW frequency was set to 2860MHz and modulated at 1KHz. The magnetic sensitivity of this particular sample is $8.6\mu T/\sqrt{Hz}$

to suppress low-frequency noise from the laser. The measurement was repeated ten times at each magnetic field to generate error bars. From this plot, we can calculate the layers sensitivity to be around $8.6\mu T/\sqrt{Hz}$. A more relevant number would be the sensitivity per $\sqrt{volume}$ which we can calculate using the estimated value for thickness and we get $125nT\mu m^{3/2}/\sqrt{Hz}$ .

## 5.7 Projection of Sensitivity to Magnetic Field Sources

Following the discussion in chapter 2, even though the magnetic sensitivity might not be very high, these shallow layers have a good sensitivity to nano-scale magnetic field sources. In figures (5.8 and 5.9) we project the sensitivity to a current running in a long wire on the diamond's surface. In figures (5.10 and 5.11) we project the sensitivity of our layers to a magnetic dipole on the diamond surface.

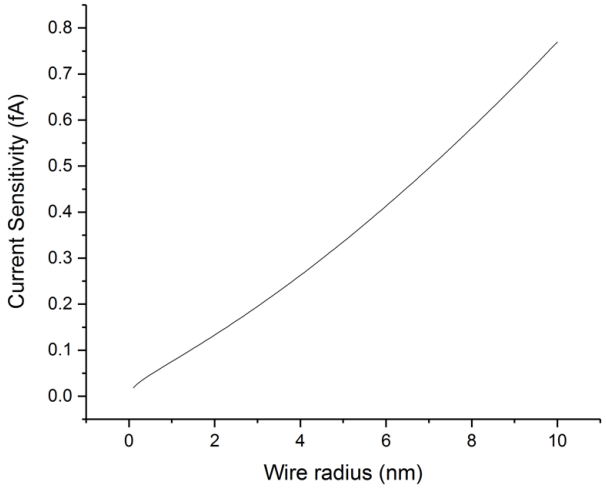


Figure 5.8: Projection of current sensitivity for our shallow layers for wires with radii less than 10nm

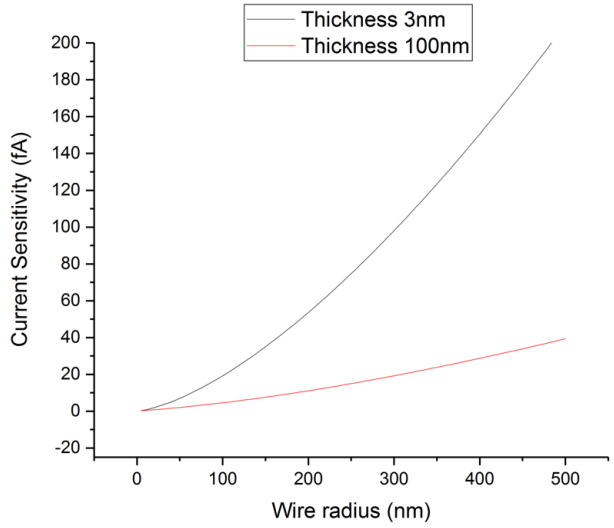


Figure 5.9: Comparison of projected current sensitivity for our shallow layers (black) and for similar layers with thickness of 100nm (red)

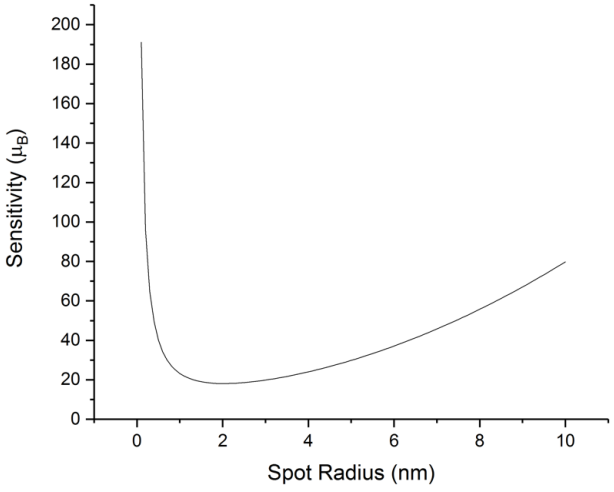


Figure 5.10: Projection of sensitivity to magnetic dipoles for our shallow layers for super resolution experiments

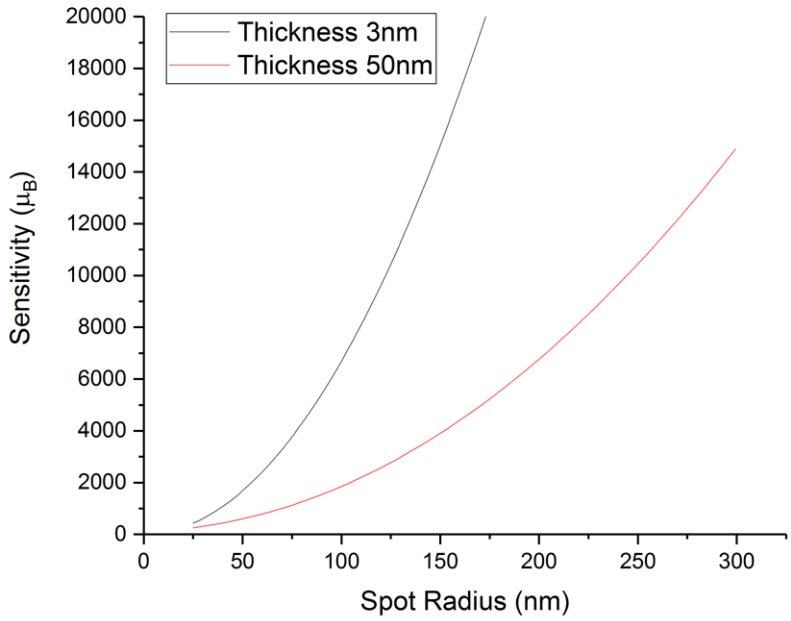


Figure 5.11: Comparison of projected sensitivity to magnetic dipoles for our shallow layers (black) and for similar layer with thickness 50nm for experiments with resolution comparable to the classical diffraction limit

# 6. NANODIAMOND GROWTH RESULTS

Even though bulk diamonds usually have higher quality than nanodiamonds, they are not suitable for all applications. A shallow layer of NVs on a bulk crystal can provide a two-dimensional map of magnetic field sources whereas nanodiamonds can produce three-dimensional maps. Another advantage is that nanodiamonds can be used deeper in substrates or tissues for application where the magnetic field source cannot be brought to the surface of a bulk diamond. In this document growth procedure will not be discussed in details, only analysis of the growth product is presented.

## 6.1 HPHT

In this experiment, the growth was attempted at conditions below the self-nucleation threshold. We choose 1-adamantylamine as the seed molecule. If the seeded growth is successful, the nanodiamonds will contain a nitrogen defect in it which can be transformed into an NV center through annealing and electron irradiation.

The product of this growth experiment was loaded on a silicon TEM grid that can withstand high-temperature annealing. First, the sample was investigated under the confocal microscope figure(6.1a). The optical spectrum shows a peak at 630nm which corresponds to an unknown defect in diamond [20]. Then, the sample was investigated under TEM and we obtained the diffraction spectrum of the particle as further proof that the particles are indeed diamonds figure(6.2). Using the TEM, the diamond nanoparticles were irradiated with a dose of $6.8 \times 10^{20} e/cm^2$ at 800C. Then, the sample was loaded again to the confocal microscope and optical spectrum of the NV was observed figure(6.3). While studying the particles under the confocal microscope the optical spectrum changed and the 630nm peak disappeared. Finally, we measured the ODMR spectra of the particle and got a dip at 2870 MHz which matches that of NVs figure(6.4).

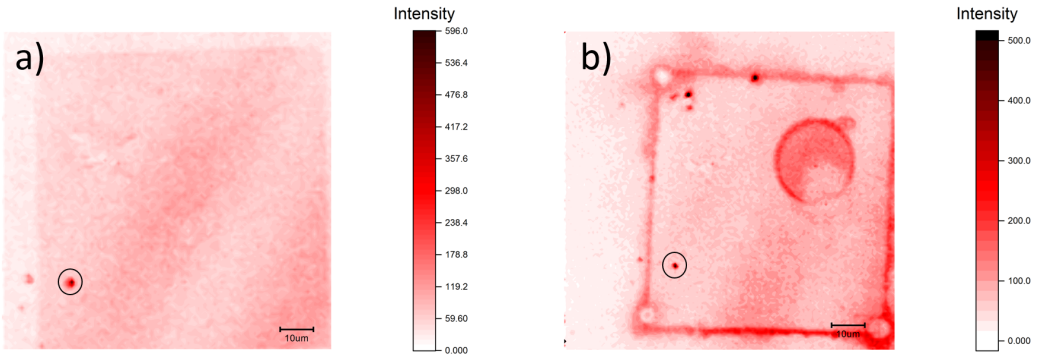


Figure 6.1: Confocal images for the product of an HPHT seeded growth experiment a) before high temprature electron irradiation and b)after. black circle indicate the diamond location.

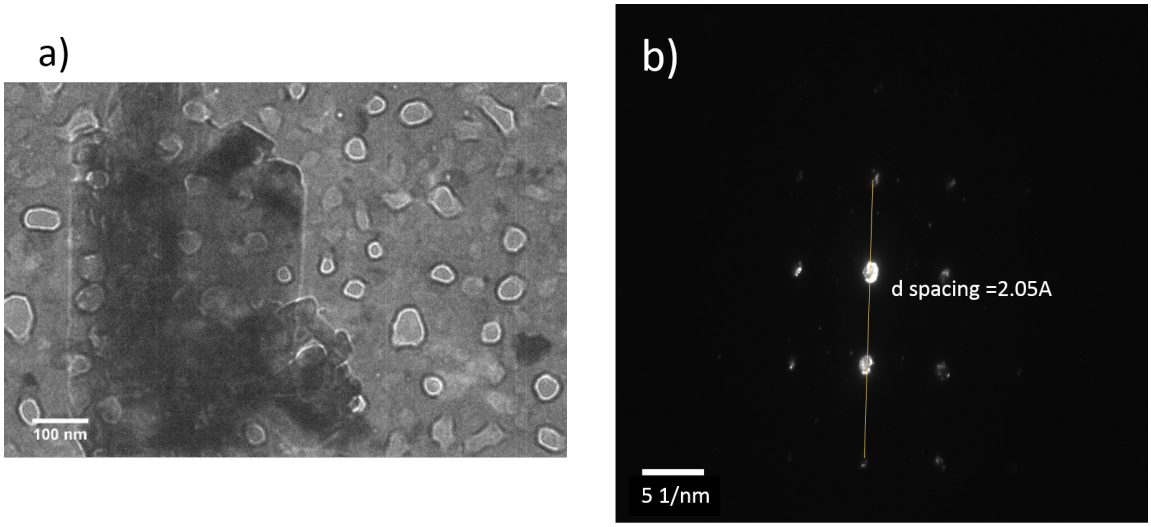


Figure 6.2: TEM a)image and b)diffraction pattern of the product of the HPHT experiment

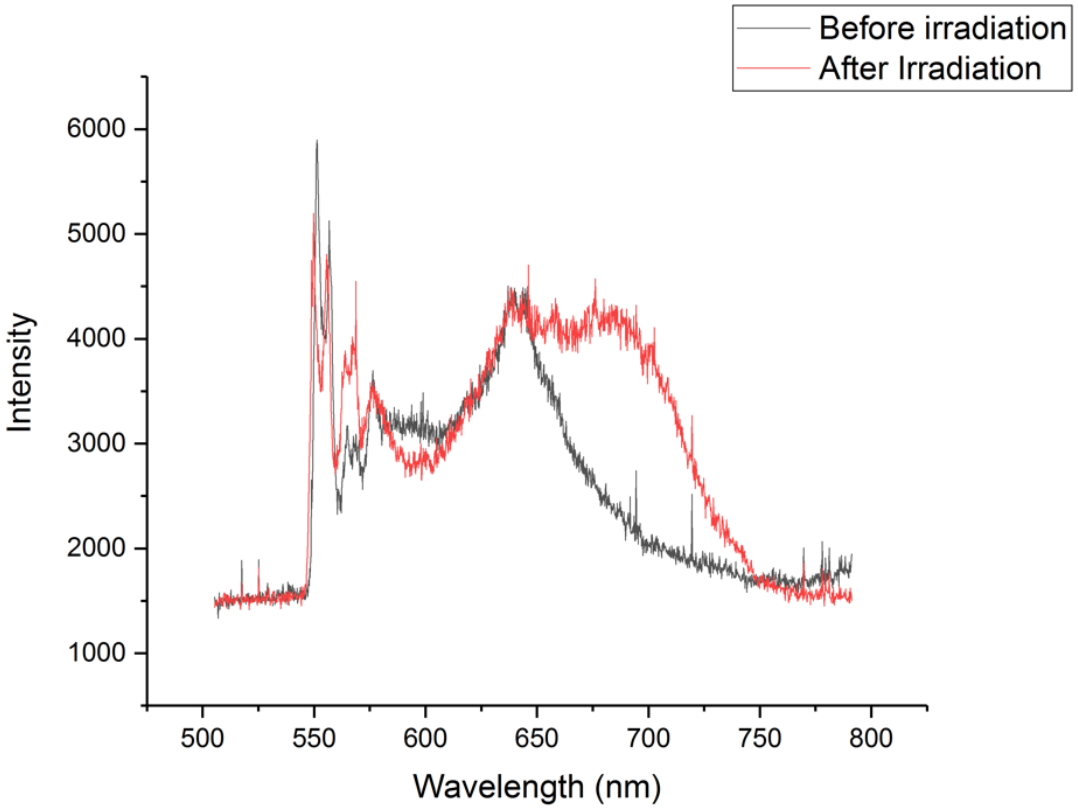


Figure 6.3: Optical spectrum before(black) and after(red) electron irradiation. HPHT experiment

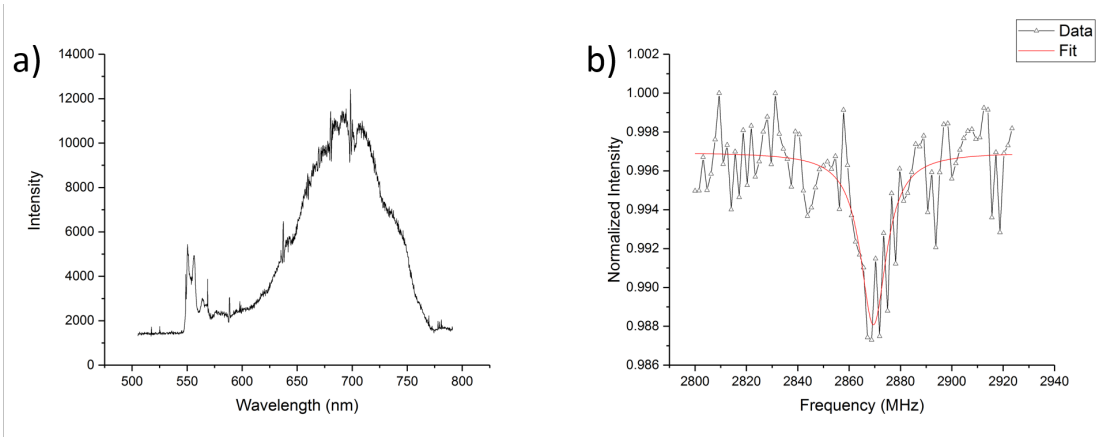


Figure 6.4: a) Optical spectrum and b) ODMR spectrum for the product of the HPHT seeded growth experiment

## 6.2 MW Plasma

We have not attempted seeded growth with our plasma CVD system yet. So far we have successfully grown diamond through self-nucleation using dichloromethane as the fuel. We have also successfully grown nanodiamonds with nitrogen defects by mixing the fuel with trimethylamine. The growth product was loaded on a lacy carbon TEM grid and inserted to the electron microscope. The TEM images show many diamond nanoparticles with a wide range of diameters from 0 to 50nm figure(6.5) We have also obtained a diffraction pattern which clearly shows the expected pattern of diamond figure(6.5c).

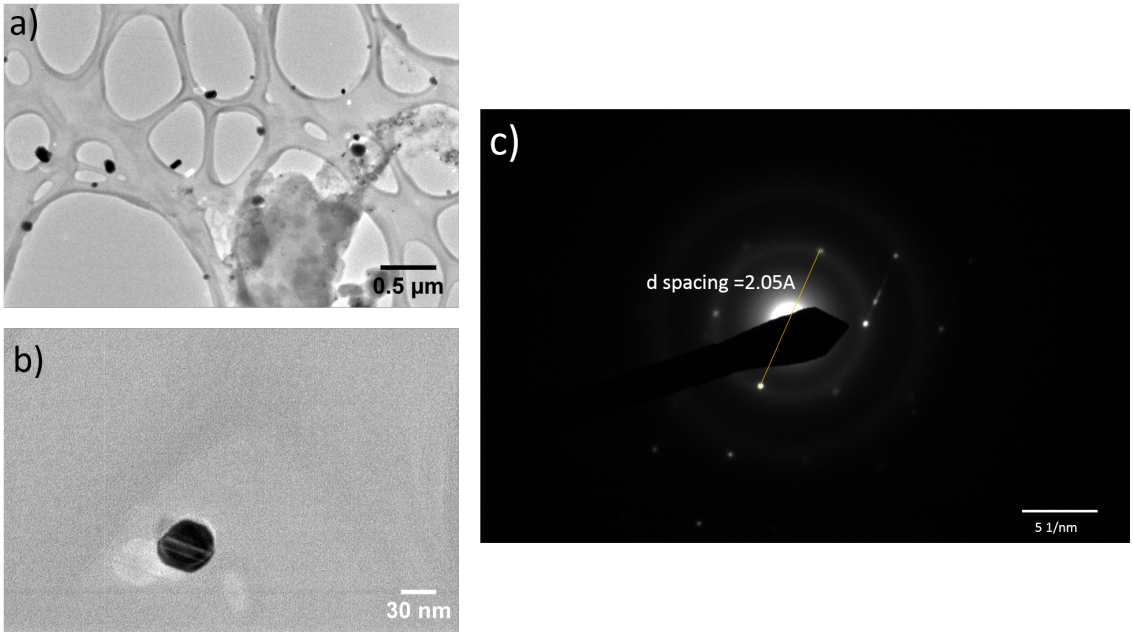


Figure 6.5: a) Low magnification TEM image for the product of the plasma CVD growth experiment, b) zoom in one particle with diameter of around 30nm, c) diffraction pattern of the particle in b showing the diamond's 2.05A spacing.

Finally, the sample was irradiated using TEM with dose $7.9\times10^{18}e/cm^2$ at temperature 740C. The diamonds were not fluorescent until after high-temperature electron irradiation.

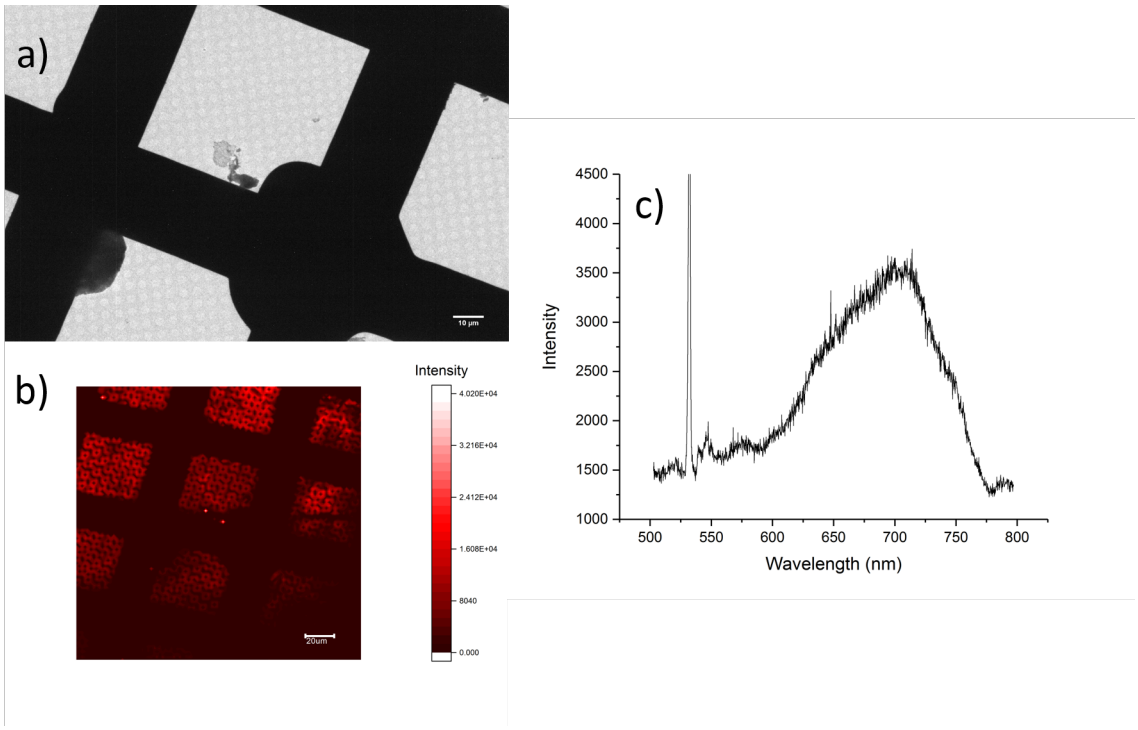


Figure 6.6: Results for electron irradiation of the product of the plasma CVD growth experiment a) electron microscope image of the irradiated area in the center of the image b) Optical image of the irradiated area showing a few bright spots. c) Optical spectrum for one of the bright particles in b.

This is an indication that the diamond quality is good since it does not contain many vacancies. After the electron irradiation, we verified that NVs were created by collecting the optical spectrum figure(5.6). we also measured the ODMR spectrum which has a peak at around 2850 MHz figure(6.7). The ODMR spectrum is shifted from that of the NV by around 20 MHz. This shift has not yet been explained.

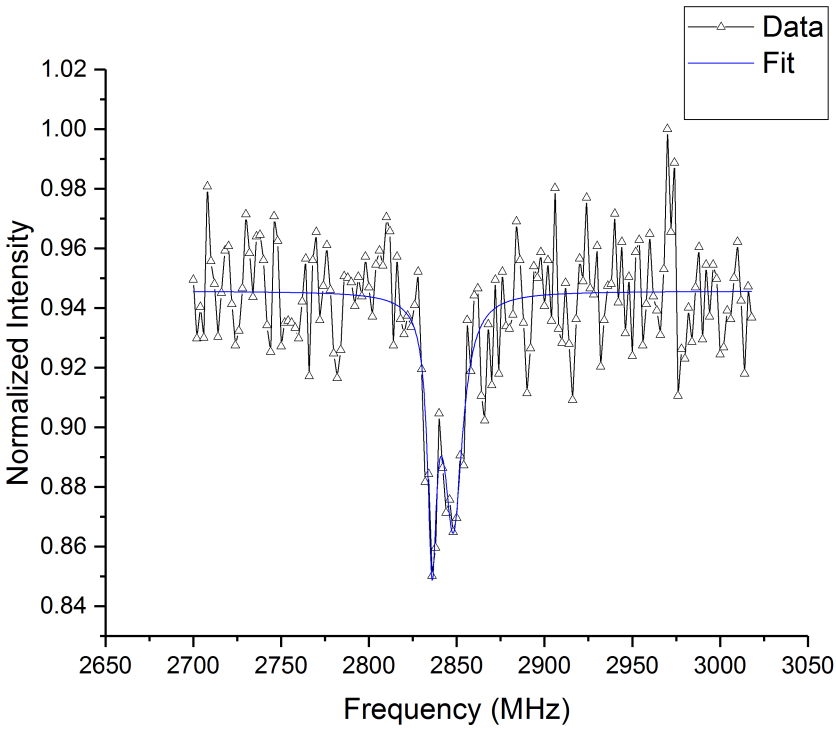


Figure 6.7: ODMR spectrum for the product of the plasma CVD growth experiment after electron irradiation.

# 7. SUMMARY

In this work, we are trying to solve the problem of sensing nano-scale magnetic field sources. First, we established the differences between magnetic field sensitivity and sensitivity to magnetic field sources. We discussed in details the geometrical effects of the NV ensemble in terms of depth, spatial resolution and thickness on the sensitivity for two examples, a current in a long wire and a magnetic dipole.

One way to get the NVs in close proximity to a nano-scale source is through shallow implantation in bulk diamond. We utilize PIII implantation technique which has the advantage of simultaneous implantation and etching. Using a type Ib diamond and implanting at high temperature we were able to create a bright layer of NVs approximately 2nm below the diamond surface. We measure a magnetic sensitivity of around $125nT\mu m^{3/2}/\sqrt{Hz}$ for these layers, which is decent considering the quality of the diamond substrate we started with. However, since the layer is very shallow, we project a sensitivity of sub $fA/\sqrt{Hz}$ for a current running in a wire of radius < 10nm on the surface of the diamond.

Another way to create a shallow sensor using NVs is through nanodiamond growth. We focused on developing seeded growth technique which has the advantage of producing higher quality diamond among other interesting advantages. So far we have attempted seeded growth using HPHT technique only. We showed seeded growth nanodiamond by growing the particles around a seed molecule which contains one nitrogen atom. After electron irradiation and annealing these diamond showed the NV fluorescence spectrum as well as the NV's ODMR spectrum.

We are also developing nanodiamond growth using MW plasma CVD technique. Although we have not yet attempted seeded growth, we were successful in growing good quality nitrogen doped nanodiamonds. After electron irradiation and annealing those

nanoparticles showed the NV fluorescence spectrum as well as the NV's ODMR spectrum.

# REFERENCES


[1] W. C. Griffith, S. Knappe, and J. Kitching, "Femtotesla atomic magnetometry in a microfabricated vapor cell," *Optics Express*, vol. 18, no. 26, pp. 27167–27172, 2010.

[2] H. B. Dang, A. C. Maloof, and M. V. Romalis, "Ultrahigh sensitivity magnetic field and magnetization measurements with an atomic magnetometer," *Applied Physics Letters*, vol. 97, no. 15, p. 151110, 2010.

[3] D. Drung, C. Assmann, J. Beyer, A. Kirste, M. Peters, F. Ruede, and T. Schurig, "Highly sensitive and easy-to-use squid sensors," *IEEE Transactions on Applied Superconductivity*, vol. 17, no. 2, pp. 699–704, 2007.

[4] A. Finkler, D. Vasyukov, Y. Segev, L. Ne'eman, E. O. Lachman, M. L. Rappaport, Y. Myasoedov, E. Zeldov, and M. E. Huber, "Scanning superconducting quantum interference device on a tip for magnetic imaging of nanoscale phenomena," *Review of Scientific Instruments*, vol. 83, no. 7, p. 073702, 2012.

[5] P. Pai, L. Y. Chen, and M. Tabib-Azar, "Fiber optic magnetometer with sub-pico tesla sensitivity for magneto-encephalography," *2014 IEEE Sensors*, pp. 722–725, 2014.

[6] M. N. Deeter, G. W. Day, T. J. Beahn, and M. Manheimer, "Magnetooptic magnetic-field sensor with 1.4pt/root(hz) minimum detectable field at 1 khz," *Electronics Letters*, vol. 29, no. 11, pp. 993–994, 1993.

[7] M. Loretz, S. Pezzagna, J. Meijer, and C. L. Degen, "Nanoscale nuclear magnetic resonance with a 1.9-nm-deep nitrogen-vacancy sensor," *Applied Physics Letters*, vol. 104, no. 3, p. 033102, 2014.

[8] T. Wolf, P. Neumann, K. Nakamura, H. Sumiya, T. Ohshima, J. Isoya, and J. Wrachtrup, "Subpicotesla diamond magnetometry," *Physical Review X*, vol. 5,

no. 4, p. 041001, 2015.

[9] C. L. Degen, M. Poggio, H. J. Mamin, C. T. Rettner, and D. Rugar, "Nanoscale magnetic resonance imaging," *Proceedings of the National Academy of Sciences of the United States of America*, vol. 106, no. 5, pp. 1313–1317, 2009.

[10] A. O. Sushkov, I. Lovchinsky, N. Chisholm, R. L. Walsworth, H. Park, and M. D. Lukin, "Magnetic resonance detection of individual proton spins using quantum reporters," *Physical Review Letters*, vol. 113, no. 19, p. 197601, 2014.

[11] J. F. Barry, M. J. Turner, J. M. Schloss, D. R. Glenn, Y. Song, M. D. Lukin, H. Park, and R. L. Walsworth, "Optical magnetic detection of single-neuron action potentials using quantum defects in diamond," *Proceedings of the National Academy of Sciences of the United States of America*, vol. 113, no. 49, pp. 14133–14138, 2016.

[12] S. J. DeVience, L. M. Pham, I. Lovchinsky, A. O. Sushkov, N. Bar-Gill, C. Belthangady, F. Casola, M. Corbett, H. L. Zhang, M. Lukin, H. Park, A. Yacoby, and R. L. Walsworth, "Nanoscale nmr spectroscopy and imaging of multiple nuclear species," *Nature Nanotechnology*, vol. 10, no. 2, pp. 129–134, 2015.

[13] G. Balasubramanian, P. Neumann, D. Twitchen, M. Markham, R. Kolesov, N. Mizuochi, J. Isoya, J. Achard, J. Beck, J. Tissler, V. Jacques, P. R. Hemmer, F. Jelezko, and J. Wrachtrup, "Ultralong spin coherence time in isotopically engineered diamond," *Nature Materials*, vol. 8, no. 5, pp. 383–387, 2009.

[14] S. Arroyo-Camejo, M. P. Adam, M. Besbes, J. P. Hugonin, V. Jacques, J. J. Greffet, J. F. Roch, S. W. Hell, and F. Treussart, "Stimulated emission depletion microscopy resolves individual nitrogen vacancy centers in diamond nanocrystals," *Acs Nano*, vol. 7, no. 12, pp. 10912–10919, 2013.

[15] K. Ohashi, T. Rosskopf, H. Watanabe, M. Loretz, Y. Tao, R. Hauert, S. Tomizawa, T. Ishikawa, J. Ishi-Hayase, S. Shikata, C. L. Degen, and K. M. Itoh, "Negatively charged nitrogen-vacancy centers in a 5 nm thin c-12 diamond film," *Nano Letters*, vol. 13, no. 10, pp. 4733–4738, 2013.

[16] J. C. Bourgoin and B. Massarani, "Threshold energy for atomic displacement in diamond," *Physical Review B*, vol. 14, no. 8, pp. 3690–3694, 1976.

[17] N. Aslam, G. Waldherr, P. Neumann, F. Jelezko, and J. Wrachtrup, "Photo-induced ionization dynamics of the nitrogen vacancy defect in diamond investigated by single-shot charge state detection," *New Journal of Physics*, vol. 15, no. 1, p. 013064, 2013.

[18] S. Waldchen, J. Lehmann, T. Klein, S. van de Linde, and M. Sauer, "Light-induced cell damage in live-cell super-resolution microscopy," *Scientific Reports*, vol. 5, p. 15348, 2015.

[19] J. Tisler, R. Reuter, A. Lammle, F. Jelezko, G. Balasubramanian, P. R. Hemmer, F. Reinhard, and J. Wrachtrup, "Highly efficient fret from a single nitrogen-vacancy center in nanodiamonds to a single organic molecule," *Acs Nano*, vol. 5, no. 10, pp. 7893–7898, 2011.

[20] K. Bray, R. Sandstrom, C. Elbadawi, M. Fischer, M. Schreck, O. Shimoni, C. Lobo, M. Toth, and I. Aharonovich, "Localization of narrowband single photon emitters in nanodiamonds," *Acs Applied Materials  Interfaces*, vol. 8, no. 11, pp. 7590–7594, 2016.